Tightly Coupled Inertial Navigation System With Signals of Opportunity Aiding

JOSHUA J. MORALES, Member, IEEE

ZAHER M. KASSAS, Senior Member, IEEE
University of California Irvine, CA USA

A tightly coupled inertial navigation system (INS) aided by ambient signals of opportunity (SOPs) is developed. In this system, a navigating vehicle aids its onboard INS using pseudoranges drawn from terrestrial SOPs with unknown emitter positions and clock biases through an extended Kalman filter-based radio simultaneous localization and mapping (SLAM) framework. The SOP-aided INS uses both global navigation satellite system (GNSS) and SOP pseudoranges during GNSS availability periods and switches to using SOP pseudoranges exclusively during GNSS unavailability periods. This framework is studied through numerical simulations by varying: 1) Quantity of exploited SOPs and 2) quality of SOP-equipped oscillators. It is demonstrated that the SOP-aided INS using a *consumer-grade* IMU produces smaller estimation uncertainties compared to a traditional tightly coupled GNSS-aided INS using a *tactical-grade* IMU. In the absence of GNSS signals, over the simulation finite-time horizon, the errors produced by the SOP-aided INS appear to be bounded, while the errors produced by a traditional tightly coupled GNSS-aided INS diverge unboundedly. Moreover, the article presents experimental results demonstrating an unmanned aerial vehicle using terrestrial cellular SOPs to aid its onboard consumer-grade IMU in the absence of GNSS signals. It is demonstrated that the final position error of a traditional tightly coupled GNSS-aided INS after 30 s of GNSS cutoff was 57.30 m, while the final position error of the tightly coupled SOP-aided INS was 9.59 m.

I. INTRODUCTION

Today's navigation systems, particularly those onboard ground and aerial vehicles, fuse information from a global navigation satellite system (GNSS) receiver and an inertial measurement unit (IMU). The integration of these two systems, typically referred to as a GNSS-aided inertial navigation system (INS), takes advantage of the complementary properties of each system: The long-term stability of a GNSS navigation solution aids the short-term accuracy of an INS. However, relying on GNSS alone to aid an INS poses an alarming vulnerability: GNSS signals could become unavailable or unreliable, such as in deep urban canyons [1] or in environments under a malicious cyber attack (e.g., jamming or spoofing) [2]. Without GNSS aiding, the errors in the INS will accumulate and eventually diverge, compromising the vehicle's safe and efficient operation. Consumer and small-size applications that use affordable microelectromechanical systems (MEMS)-based IMUs are particularly susceptible to large error divergence rates. While higher quality IMUs may reduce the rate of error divergence, they may violate cost, size, weight, and/or power constraints.

Current trends to supplement a navigation system in the event that GNSS signals become unreliable are traditionally sensor based (e.g., cameras [3], lasers [4], sonar [5], and odometers [6]). These sensors could be used to extract *relative* motion information to reduce the INS's error divergence rate. However, they are still dead-reckoning (DR)-type sensors; therefore, during prolonged periods of GNSS outage, the error will eventually diverge. Moreover, these sensors only provide *local* position estimates, may not properly function in all environments (e.g., fog, snow, rain, dust, nighttime, etc.), and are still susceptible to malicious attacks [7].

Recently, signals of opportunity (SOPs) have been considered to enable navigation whenever GNSS signals become unavailable or unreliable [8]. SOPs are ambient radio signals that are not intended for navigation or timing purposes, such as AM/FM radio [9]–[11], cellular [12]–[16], digital television [17]–[19], low Earth orbit (LEO) satellite signals [20]–[25], and Wi-Fi [26], [27]. In contrast to the aforementioned DR-type sensors, *absolute* position information may be extracted from SOPs to provide bounded INS errors. Moreover, SOPs are practically unaffected by dense smoke, fog, rain, snow, and other poor weather conditions.

SOPs enjoy several inherently desirable attributes for navigation purposes: 1) Abundance in most locales of interest, 2) transmission at a wide range of frequencies and directions, 3) reception at carrier-to-noise ratio that is commonly tens of dBs higher than that of GNSS signals, and 4) they are free to use, since their infrastructure is already operational. However, unlike GNSS, whose satellite states are transmitted in their navigation message, the states of

Manuscript received October 18, 2019; revised February 14, 2020, October 6, 2020, and December 28, 2020; released for publication December 29, 2020. Date of publication January 25, 2021; date of current version June 9, 2021.

DOI. No. 10.1109/TAES.2021.3054067

Refereeing of this contribution was handled by Y. Wu.

This work was supported in part by the Office of Naval Research (ONR) under Grant N00014-16-1-2305 and in part by the National Science Foundation (NSF) under Grant 1929965.

Authors' addresses: Joshua J. Morales was with University of California Riverside, CA 92501 USA and is now with StarNav LLC Riverside, CA 92501 USA, E-mail: (joshua.morales@ieee.org); Zaher M. Kassas is with the Department of Mechanical and Aerospace Engineering, the University of California Irvine, CA 92697 USA, E-mail: (zkassas@ieee.org). *(Corresponding author: Zaher M. Kassas.)*

This article has supplementary downloadable material available at http://ieeexplore.ieee.org, provided by the authors. This includes a video file of the experimental demonstration. This material is 74 MB in size.

SOPs, namely, their position and clock states, are typically unknown *a priori* and must be estimated.

The literature on SOPs answers theoretical observability and estimability questions [28], [29] and prescribes receiver trajectories for accurate receiver and SOP localization and timing estimation [30], [31]. Moreover, recent work have investigated SOP dynamic clock models [32] and have demonstrated meter-level accurate navigation with SOPs on ground vehicles [23], [33]–[36] and centimeter-level accurate navigation on aerial vehicles [37], [38]. With appropriately designed navigation receivers and estimation frameworks, SOPs have been exploited as an INS aiding source [39], [40].

This article presents an extended Kalman filter (EKF)-based radio simultaneous localization and mapping (SLAM) framework, where the states of *unknown* terrestrial SOPs are simultaneously estimated along with the states of the navigating vehicle. Terrestrial SOP pseudoranges are used to aid the vehicle's INS and simultaneously map unknown SOPs. This estimation problem is analogous to the SLAM problem in robotics [41]. However, in contrast to the environmental map of the typical SLAM problem, which is composed of static states (position of walls, poles, trees, etc.); the radio SLAM map is composed of both static states (SOP positions) and dynamic stochastic states (SOP clock bias and drift).

Radio SLAM-type frameworks have been adopted to exploit unknown SOPs for navigation as a standalone alternative to GNSS [42]. However, only the initial navigating vehicle's position and the unknown SOPs' positions and clock biases were estimated using SOP pseudoranges drawn over the vehicle's traversed trajectory and a simple linear dynamics model was employed. EKF-based SOP-aided INS frameworks that estimated the entire vehicle's trajectory, clock bias, INS errors, and SOPs' states using incoming measurements were developed and studied in [43] and [44]. In contrast to prior work presenting EKF-based SOP-aided INS frameworks, this article provides a self-contained treatment of an aided INS, with sufficient details for the interested reader to implement an SOP-aided INS that operates both when GNSS is available and when GNSS becomes unavailable or unreliable. The developed framework will focus on the use of consumer-grade and tactical-grade IMUs; therefore, the EKF will estimate "absolute" INS states (e.g., orientation, position, velocity). This is in contrast to an aided INS with a navigation-grade IMU, where the purpose of an EKF is to estimate the INS errors, which are then fed back to the INS to keep the errors small (and thus linear).

To evaluate the performance of the developed SOP-aided INS framework, this article presents a sensitivity study conducted through numerical simulations, by varying the quantity and quality of exploited SOPs. Moreover, this article presents experimental results demonstrating an unmanned aerial vehicle (UAV) using terrestrial cellular SOPs to aid its onboard consumer-grade IMU in the absence of GNSS signals. During GNSS outages, the UAV's position errors appear to be bounded over the simulation and experimental finite-time horizon; although no analytical proof was established for the infinite-time horizon case. It is demonstrated that the final position error of a traditional tightly coupled GNSS-aided INS after 30 s of GNSS cutoff was 57.30 m, while the final position error of the tightly coupled SOP-aided INS was 9.59 m.

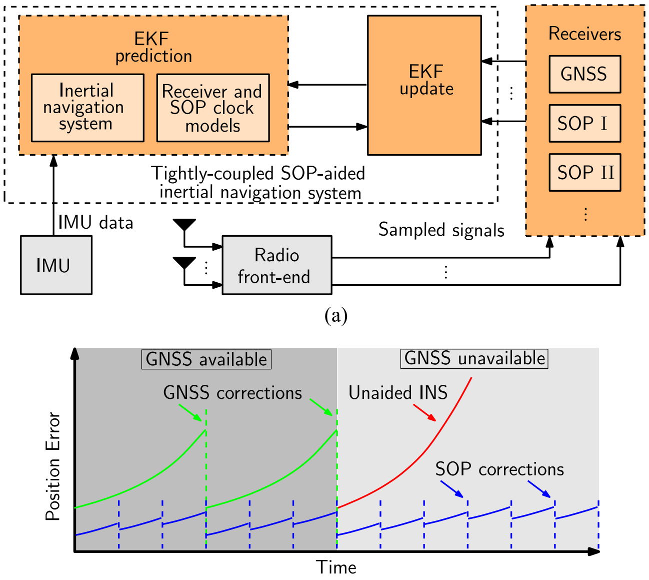

(a)

(b)

Fig. 1. (a) High-level diagram of an EKF-based tightly coupled INS aided by GNSS (when available) and different SOPs, denoted SOP I, SOP II and (b) Conceptual illustration comparing the resulting position errors for: Traditional GNSS-aided INS (green), SOP-aided INS (blue), and unaided INS (red).

The remainder of this article is organized as follows. Section II provides a high-level description of the SOP-aided INS framework developed in this article. Section III overviews the main components of an aided INS. Section IV describes the radio SLAM SOP-aided INS framework. Section V presents simulation results comparing the estimation performance of the SOP-aided INS using a consumer-grade IMU with a traditional GNSS-aided INS using a tactical-grade IMU. It also presents a performance sensitivity analysis of the SOP-aided INS framework over varying quantity and quality of exploited SOPs. Section VI presents experimental results demonstrating a UAV navigating with cellular SOPs using the SOP-aided INS framework. Finally, Section VII concludes the article.

II. PROBLEM DESCRIPTION

A high-level block diagram of the developed EKF-based radio SLAM framework to aid a navigating vehicle's INS with SOP pseudoranges is illustrated in Fig. 1(a). When GNSS signals are available, *both* GNSS and SOP receivers produce pseudoranges that are sent to an EKF update step to simultaneously aid the INS and estimate the unknown SOPs' states. When GNSS signals become unavailable, SOP pseudoranges are used *exclusively* to continue aiding the INS and refine the SOPs' state estimates. Fig. 1(b) is a conceptual illustration comparing the resulting position errors for a traditional GNSS-aided INS (green), SOP-aided INS (blue), and unaided INS (red). Note that when GNSS signals are available, the SOP-aided INS is expected to produce lower position estimation errors compared to a traditional GNSS-aided INS. This is primarily due to a reduction in the vertical dilution of precision (VDOP) over using GNSS alone when terrestrial SOP pseudoranges, which have small elevation angles, are used with GNSS pseudoranges, which inherently have larger elevation angles [45]. In [13], experimental results show a UAV's position estimation uncertainty ellipsoid reduce by 84% compared to using Global Positioning System (GPS) pseudoranges alone when seven GPS satellites' and five SOPs' pseudoranges were used together to estimate the position of the UAV. When GNSS signals become unavailable, a bound on the SOP-aided INS position errors is expected [29], [46], whereas the unaided INS errors are expected to diverge.

III. OVERVIEW OF AIDED INERTIAL NAVIGATION

An aided inertial navigation system consists of three main components: 1) IMU, 2) INS processor, and 3) aiding sensors and corresponding fusion filter. This section overviews these components.

A. Inertial Measurement Unit

An IMU typically consist of a triad-gyroscope and triad-accelerometer, which produce rotation rate and specific force measurements, respectively, along three coordinate axes. These measurements are corrupted by noise as well as static and dynamic stochastic errors (e.g., biases, scale factors, cross-coupling, and cross-axis sensitivity). A DR-based navigation solution integrates these corrupted measurements over time, which causes the navigation solution to undesirable drift. Therefore, it is important to "clean up" these measurements, as much as possible, before they get integrated through an INS. The IMU's onboard processor removes factory-calibrated static errors; however, dynamic and stochastic error components (known as in-run errors), should be modeled and estimated online. It is within the discretion of the navigation filter designer to determine which errors should be modeled and estimated by considering the navigation system's processing power, IMU's quality, and maneuvers that the IMU is expected to undertake. To avoid convoluting the forthcoming discussion, only random noise and the gyroscope's and accelerometer's biases are modeled. Additional details of IMU errors and methods to determine which states should be estimated are discussed in [47]–[49].

Noise-corrupted and bias-corrupted IMU measurements can be modeled in discrete-time as

$$ {}^{b}\boldsymbol{\omega}_{\text{imu}}(k) = {}^{b}\boldsymbol{\omega}_{i}(k) + \boldsymbol{b}_{\text{gyr}}(k) + \boldsymbol{n}_{\text{gyr}}(k), \quad k = 1, 2, \ldots \tag{1} $$

$$ \begin{aligned} {}^{b}\mathbf{a}_{\text{imu}}(k) = {}^{b}_{i}\mathbf{R}(k)\left[{}^{i}\mathbf{a}_{b}(k) - {}^{i}\boldsymbol{g}(k, {}^{i}\boldsymbol{r}_{b}(k))\right] + \boldsymbol{b}_{\text{acc}}(k) \\ + \boldsymbol{n}_{\text{acc}}(k) \end{aligned} \tag{2} $$

where ${}^{b}\boldsymbol{\omega}_{i} \in \mathbb{R}^3$ is the true rotation rate of a coordinate frame $\{b\}$ fixed to the body of the IMU with respect to an inertial frame $\{i\}$, such as the Earth-centered inertial (ECI) frame; $\boldsymbol{b}_{\text{gyr}} \in \mathbb{R}^3$ is the gyroscope's three-dimensional (3D) bias; $\boldsymbol{n}_{\text{gyr}} \in \mathbb{R}^3$ is a measurement noise vector, which is modeled as a white noise sequence with covariance $\mathbf{Q}_{\boldsymbol{n}_{\text{gyr}}}$; ${}^{b}_{i}\mathbf{R} \in \mathbb{R}^{3\times3}$ is the rotation matrix, which rotates the coordinates of a vector expressed in frame $\{i\}$ into frame $\{b\}$; ${}^{i}\mathbf{a}_{b} \in \mathbb{R}^3$ is the true acceleration of $\{b\}$ expressed in $\{i\}$; ${}^{i}\boldsymbol{g} \in \mathbb{R}^3$ is the acceleration due to gravity in the inertial frame, which depends on the position of the IMU ${}^{i}\boldsymbol{r}_{b} \in \mathbb{R}^3$; $\boldsymbol{b}_{\text{acc}} \in \mathbb{R}^3$ is the accelerometer's 3D bias; and $\boldsymbol{n}_{\text{acc}} \in \mathbb{R}^3$ is a measurement noise vector, which is modeled as a white noise sequence with covariance $\mathbf{Q}_{\boldsymbol{n}_{\text{acc}}}$. Fig. 2 illustrates the relationships of the position and orientation of $\{b\}$ with respect to $\{i\}$ for an aerial vehicle-mounted IMU. The evolution of the gyroscope and accelerometer biases are modeled as random walks as

$$ \boldsymbol{b}_{\text{gyr}}(k+1) = \boldsymbol{b}_{\text{gyr}}(k) + \boldsymbol{w}_{\text{gyr}}(k) \tag{3} $$

$$ \boldsymbol{b}_{\text{acc}}(k+1) = \boldsymbol{b}_{\text{acc}}(k) + \boldsymbol{w}_{\text{acc}}(k) \tag{4} $$

where $\boldsymbol{w}_{\text{gyr}}$ and $\boldsymbol{w}_{\text{acc}}$ are process noise vectors that drive the in-run bias variation (or bias instability) and are modeled as white noise sequences with covariance $\mathbf{Q}_{\boldsymbol{w}_{\text{gyr}}}$ and $\mathbf{Q}_{\boldsymbol{w}_{\text{acc}}}$, respectively. Note that other models may be used in place of (3) and (4), e.g., a common model is to use a Gauss–Markov process to model the slow varying bias, which is parameterized by a time constant and is driven by white noise [48], [49]. The measurements (1) and (2) are sent to the INS to produce an orientation, velocity, and position solution, as discussed next.

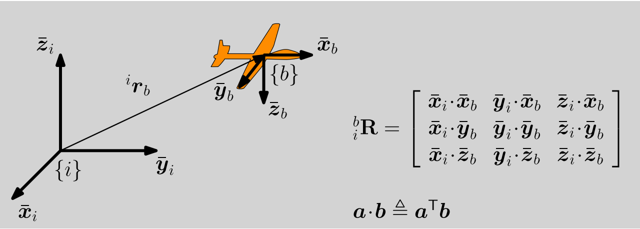

Fig. 2. Position ${}^{i}\boldsymbol{r}_b$ of the origin of coordinate frame $\{b\}$ expressed in coordinate frame $\{i\}$. The rotation matrix ${}^{b}_{i}\mathbf{R}$ rotates the coordinates of a vector expressed in frame $\{i\}$ into frame $\{b\}$. The notation $\boldsymbol{a}\cdot\boldsymbol{b}$ denotes the inner product of vectors $\boldsymbol{a}$ and $\boldsymbol{b}$. The principal directions of $\{i\}$ and $\{b\}$ are represented by the unit vectors $\bar{\boldsymbol{x}}_i, \bar{\boldsymbol{y}}_i, \bar{\boldsymbol{z}}_i$ and $\bar{\boldsymbol{x}}_b, \bar{\boldsymbol{y}}_b, \bar{\boldsymbol{z}}_b$, respectively. Note that the describing frame leading superscript on these unit vectors has been omitted, since the frame used to describe these vectors is arbitrary when computing ${}^{b}_{i}\mathbf{R}$, as long as they are all described in the same frame.

B. Inertial Navigation System

There are two main INS architectures: Stable platform (i.e., gimballed) and strapdown. On one hand, a stable platform INS uses a complex bulky physical structure to mechanically isolate the IMU's sensing axes from the rotational motion of the navigating vehicle. This isolation allows for direct extraction and integration of the IMU's acceleration measurements. On the other hand, a strapdown INS omits the complex bulky structure and instead uses a smaller size and lighter weight IMU, whose sensing axes are fixed to the navigating vehicle. The smaller size and

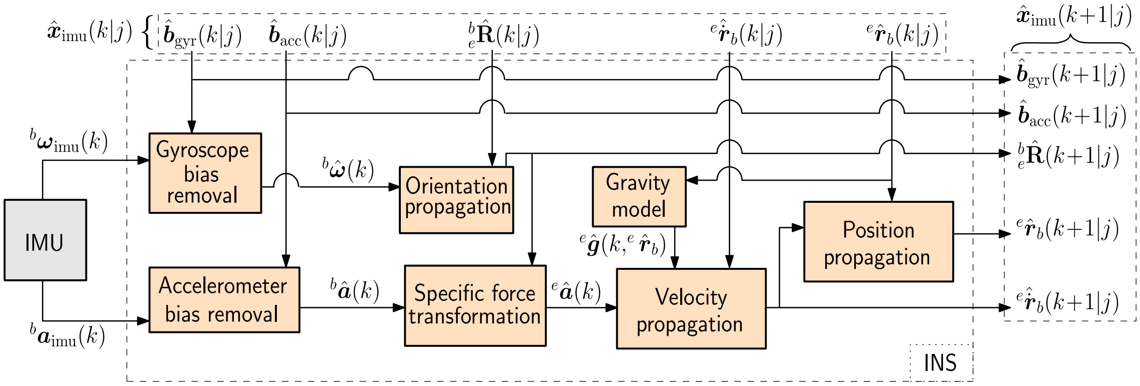

Fig. 3. Block diagram of an INS within an EKF-based aided INS. The inputs to the INS are the current state estimate $\hat{\boldsymbol{x}}_{\text{imu}}(k|j)$ and IMU measurements ${}^b\boldsymbol{a}_{\text{imu}}(k)$ and ${}^b\boldsymbol{\omega}_{\text{imu}}(k)$. The output is the one-step time update $\hat{\boldsymbol{x}}_{\text{imu}}(k+1|j)$. The internal signals ${}^b\hat{\boldsymbol{\omega}}$, ${}^e\hat{\boldsymbol{a}}$, and ${}^b\hat{\boldsymbol{a}}$, are the bias-compensated rotation rate, bias-compensated transformed specific force, and bias-compensated untransformed specific force, respectively, which are computed according to (22), (24), and (25), respectively.

lighter weight comes at the cost of additional computational complexity, which is used to resolve the IMU's sensing axes into an inertial frame before the acceleration measurements are integrated. With advances in computational power, most current navigation systems, especially those that require smaller and lighter weight sensors (e.g., small UAVs), employ a strapdown architecture. For this reason, all subsequent equations and discussions pertain to a strapdown INS; however, the SOP-aided INS developed in this article can be readily applied to a stable platform architecture by replacing strapdown mechanization equations with stable platform ones.

An INS can be used as a standalone DR system or as part of an integrated navigation system, e.g., an EKF-based aided INS, as in Fig. 1(a). The role of the INS in the context of an EKF-based aided INS is to take the sequence of sampled IMU measurements (1) and (2), extract ${}^b\boldsymbol{\omega}_i$ and ${}^i\mathbf{a}_b$, and perform successive integrations to propagate an estimate of an IMU state vector between aiding measurement updates. It is common to directly estimate the orientation, position, and velocity of the IMU in an Earth-centered Earth-fixed (ECEF) frame $\{e\}$, since aiding sources (e.g., GPS satellites and SOP emitters) are typically represented in $\{e\}$. To this end, this article develops an EKF to estimate the IMU state vector $\boldsymbol{x}_{\text{imu}} \in \mathbb{R}^{16}$, given by

$$\boldsymbol{x}_{\text{imu}} = \left[{}^b_e\bar{\boldsymbol{q}}^{\mathsf{T}},\ {}^e\boldsymbol{r}_b^{\mathsf{T}},\ {}^e\dot{\boldsymbol{r}}_b^{\mathsf{T}},\ \boldsymbol{b}_{\text{gyr}}^{\mathsf{T}},\ \boldsymbol{b}_{\text{acc}}^{\mathsf{T}} \right]^{\mathsf{T}} \tag{5}$$

where ${}^b_e\bar{\boldsymbol{q}} = [{}^b_e\boldsymbol{q}^{\mathsf{T}}, {}^b_e q_4]^{\mathsf{T}} = [{}^b_e q_1, {}^b_e q_2, {}^b_e q_3, {}^b_e q_4]^{\mathsf{T}} \in \mathbb{R}^4$ is a 4D unit quaternion, representing the IMU's orientation (i.e., rotation from frame $\{e\}$ to $\{b\}$), and ${}^e\dot{\boldsymbol{r}}_b \in \mathbb{R}^3$ is the IMU's velocity. Out of several orientation representations, the unit quaternion is selected because it provides a minimal orientation state representation and avoids singularities that Euler angles are subject to. This quaternion is related to the rotation matrix ${}^b_e\mathbf{R}$ through

$${}^b_e\mathbf{R} = \mathbf{I}_{3\times 3} - {}^b_e q_4 \lfloor {}^e_b\boldsymbol{q} \times \rfloor + 2 \lfloor {}^e_b\boldsymbol{q} \times \rfloor^2$$

where $\mathbf{I}_{3\times 3}$ denotes a 3×3 identity matrix and $\lfloor {}^e_b\boldsymbol{q} \times \rfloor$ is the skew-symmetric form of ${}^e_b\boldsymbol{q}$, which is given by

$$\lfloor {}^e_b\boldsymbol{q} \times \rfloor = \begin{bmatrix} 0 & -{}^b_e q_3 & {}^b_e q_2 \\ {}^b_e q_3 & 0 & -{}^b_e q_1 \\ -{}^b_e q_2 & {}^b_e q_1 & 0 \end{bmatrix}.$$

A block diagram of the one-step EKF time update that propagates the estimate $\hat{\boldsymbol{x}}_{\text{imu}}(k|j)$ to $\hat{\boldsymbol{x}}_{\text{imu}}(k+1|j)$ is illustrated in Fig. 3, where $\hat{\boldsymbol{x}}_{\text{imu}}(k|j) \triangleq \mathbb{E}[\boldsymbol{x}_{\text{imu}}(k)|\boldsymbol{Z}^j]$, $\mathbb{E}[\,\cdot\,|\,\cdot\,]$ is the conditional expectation operator, $\boldsymbol{Z}^j \triangleq \{z(i)\}_{i=1}^{j}$, z is a vector of INS-aiding measurements (e.g., from GNSS or SOPs), and $k \geq j$. GNSS aiding is discussed in the next subsection and SOP-aiding is discussed in the following section. The strapdown INS equations pertaining to each block are provided in Appendix A. Upon receiving an aiding measurement $z(k+1)$, the EKF performs a measurement update to produce $\boldsymbol{x}_{\text{imu}}(k+1|k+1)$, as discussed in the following subsection. If $z(k+1)$ is not available then $\boldsymbol{x}_{\text{imu}}(k+L-1|j)$ is recursively fed back to the INS to produce $\boldsymbol{x}_{\text{imu}}(k+L|j)$, where $L = 2, 3, \ldots$, until a measurement becomes available.

C. Traditional GNSS-Aided INS

A traditional EKF-based GNSS-aided INS couples the INS and GNSS through either: 1) Loose coupling, which fuses the INS and GNSS position and velocity solutions; 2) tight coupling, which fuses the INS solution with GNSS pseudoranges; or 3) deep coupling, which uses the INS solution to aid the GNSS receiver's tracking-loops [50]. This article considers tight coupling for four main reasons. First, in the event that less than four GNSS pseudoranges are available, tightly coupled systems can still provide an EKF aiding update, which is not the case in a loosely coupled system. Second, a tightly coupled system can be implemented with most commercial off-the-shelf (COTS) components, which is not the case in a deeply coupled system, since internal GNSS tracking loops are typically required. Third, the filter will optimally deal with the geometry of the aiding measurements. Fourth, the aiding source output does not have to be decimated in time (to maintain statistical independence) as a result of any filtering internal to the aiding source.

To use GNSS pseudoranges in an EKF measurement update, the receiver's clock state vector $\boldsymbol{x}_{\text{clk},r} \triangleq [\, c\delta t_{\text{r}},\ c\dot{\delta t}_{\text{r}}]^{\mathsf{T}} \in \mathbb{R}^2$ must be estimated, where δt_{r} is the receiver's clock bias, $\dot{\delta t}_{\text{r}}$ is the receiver's clock drift, and c is the speed of light. The clock dynamics is modeled as [51]

$$\boldsymbol{x}_{\text{clk,r}}(k+1) = \mathbf{F}_{\text{clk}}\boldsymbol{x}_{\text{clk,r}}(k) + \boldsymbol{w}_{\text{clk,r}}(k), \quad \mathbf{F}_{\text{clk}} = \begin{bmatrix} 1 & T \\ 0 & 1 \end{bmatrix} \tag{6}$$

where T is the sampling interval and $\boldsymbol{w}_{\text{clk,r}}$ is the process noise, which is modeled as a discrete-time white noise sequence with covariance

$$\mathbf{Q}_{\text{clk,r}} = c^2 \cdot \begin{bmatrix} S_{\tilde{w}_{\delta t,\text{r}}}T + S_{\tilde{w}_{\dot{\delta t},\text{r}}}\frac{T^3}{3} & S_{\tilde{w}_{\dot{\delta t},\text{r}}}\frac{T^2}{2} \\ S_{\tilde{w}_{\dot{\delta t},\text{r}}}\frac{T^2}{2} & S_{\tilde{w}_{\dot{\delta t},\text{r}}}T \end{bmatrix} \tag{7}$$

where $S_{\tilde{w}_{\delta t,\text{r}}}$ and $S_{\tilde{w}_{\dot{\delta t},\text{r}}}$ are the power spectra of the continuous-time process noise $\tilde{\boldsymbol{w}}_{\text{clk,r}} \triangleq [\tilde{w}_{\delta t,\text{r}},\ \tilde{w}_{\dot{\delta t},\text{r}}]^{\mathsf{T}}$, respectively [28], which can be related to the power-law coefficients, $\{h_{\alpha,\text{r}}\}_{\alpha=-2}^{2}$, which have been shown through laboratory experiments to characterize the power spectral density of the fractional frequency deviation of an oscillator from nominal frequency according to $S_{\tilde{w}_{\delta t,\text{r}}} \approx \frac{h_{0,\text{r}}}{2}$ and $S_{\tilde{w}_{\dot{\delta t},\text{r}}} \approx 2\pi^2 h_{-2,\text{r}}$ [52]. Augmenting $\boldsymbol{x}_{\text{clk,r}}$ with $\boldsymbol{x}_{\text{imu}}$ gives the GNSS-aided INS state vector $\boldsymbol{x}_{\text{gnss,ins}} \in \mathbb{R}^{18}$ that the EKF estimates, namely

$$\boldsymbol{x}_{\text{gnss,ins}} \triangleq \left[\boldsymbol{x}_{\text{imu}}^{\mathsf{T}},\ \boldsymbol{x}_{\text{clk},r}^{\mathsf{T}}\right]^{\mathsf{T}}. \tag{8}$$

The GNSS receiver makes pseudorange measurements $\{z'_{\text{gnss},n}\}_{n=1}^{N}$ at discrete-time instants to all N available GNSS satellites. After compensating for ionospheric and tropospheric delays $\{z'_{\text{gnss},n}\}_{n=1}^{N}$ is given by

$$\begin{aligned} z_{\text{gnss},n}(j) &= \|{}^e\boldsymbol{r}_b(j) - {}^e\boldsymbol{r}_{\text{gnss},n}(j)\|_2 \\ &\quad + c \cdot \left[\delta t_{\text{r}}(j) - \delta t_{\text{gnss},n}(j)\right] + v_{\text{gnss},n}(j) \end{aligned} \tag{9}$$

where $z_{\text{gnss},n} \triangleq z'_{\text{gnss},n} - c\delta t_{\text{iono},n} - c\delta t_{\text{tropo},n}$; $\delta t_{\text{iono},n}$ and $\delta t_{\text{tropo},n}$ are the ionospheric and tropospheric delays, respectively; $z'_{\text{gnss},n}$ is the uncompensated pseudorange; ${}^e\boldsymbol{r}_{\text{gnss},n}$ is the position of the nth GNSS satellite; $\delta t_{\text{gnss},n}$ is the clock bias of the nth GNSS satellite; $v_{\text{gnss},n}$ is the measurement noise, which is modeled as a discrete-time zero-mean white Gaussian sequence with variance $\sigma_{\text{gnss},n}^2$; and $j \in \mathbb{N}$ represents the time index at which $\{z_{\text{gnss},n}\}_{n=1}^{N}$ is available, which could be aperiodic. These pseudoranges $\{z_{\text{gnss},n}\}_{n=1}^{N}$ are used to filter $\hat{\boldsymbol{x}}_{\text{gnss,ins}}$ through an EKF measurement update step to produce the updated estimate $\hat{\boldsymbol{x}}_{\text{gnss,ins}}(j|j)$. Note that, to simplify the forthcoming discussion, it is assumed that the number of available GNSS satellites is constant and that the ionospheric and tropospheric errors are perfectly accounted for. In practice, so-called "range bias" states may be added to the state vector $\hat{\boldsymbol{x}}_{\text{gnss,ins}}$. Such states serve two purposes. First, estimate any residual atmospheric and multipath error for each pseudorange measurement. Second, and typically more importantly, when new or reacquired GNSS satellite measurements are added to the measurement vector, these states (along with a reset of the corresponding rows/columns of the prediction error covariance matrix) can be used to absorb the "jump" in $\hat{\boldsymbol{x}}_{\text{gnss,ins}}$ that would otherwise occur. Given the short duration of the simulation and field tests in this article, there were no constellation changes, thus the jumps were not an issue. The addition of range bias states would be prudent for longer trajectories.

Whenever GNSS pseudoranges become unavailable, the INS continues to propagate in an open-loop fashion (i.e., performing only EKF time updates). This causes the position and velocity errors to grow unboundedly with time. This is largely due to integrating the estimation errors of $\boldsymbol{b}_{\text{gyr}}$ and $\boldsymbol{b}_{\text{acc}}$, denoted $\tilde{\boldsymbol{b}}_{\text{gyr}}$ and $\tilde{\boldsymbol{b}}_{\text{acc}}$, respectively. The time evolution of the velocity estimation error ${}^e\tilde{\boldsymbol{r}}_b$ and position estimation error ${}^e\tilde{\boldsymbol{r}}_b$ after t seconds of open-loop propagation due to a constant 3D accelerometer bias error $\tilde{\boldsymbol{b}}_{\text{acc}}$ are given by [48]

$${}^e\tilde{\boldsymbol{r}}_b(t) \approx {}^e_b\mathbf{R}\tilde{\boldsymbol{b}}_{\text{acc}}t, \qquad {}^e\tilde{\boldsymbol{r}}_b(t) \approx \frac{1}{2}{}^e_b\mathbf{R}\tilde{\boldsymbol{b}}_{\text{acc}}t^2.$$

The increase of ${}^e\tilde{\boldsymbol{r}}_b$ and ${}^e\tilde{\boldsymbol{r}}_b$ with time due to a constant gyroscope bias error $\tilde{\boldsymbol{b}}_{\text{gyr}}$ is even more significant– it is squared and cubic with time, respectively. This is caused by linearly increasing orientation errors with time due to integrating $\tilde{\boldsymbol{b}}_{\text{gyr}}$. Assuming the IMU moves at a constant velocity and is level with respect to the Earth's surface, the time evolution of ${}^e\tilde{\boldsymbol{r}}_b$ and ${}^e\tilde{\boldsymbol{r}}_b$ are given by [48]

$${}^e\tilde{\boldsymbol{r}}_b(t) \approx \frac{1}{2}{}^e_b\mathbf{R}\left[\tilde{\boldsymbol{b}}_{\text{gyr}}\times\right]{}^l\boldsymbol{g}t^2, \quad {}^e\tilde{\boldsymbol{r}}_b(t) \approx \frac{1}{6}{}^e_b\mathbf{R}\left[\tilde{\boldsymbol{b}}_{\text{gyr}}\times\right]{}^l\boldsymbol{g}t^3$$

where ${}^l\boldsymbol{g} = [\,0,\ 0,\ -\|{}^e\boldsymbol{g}\|_2]^{\mathsf{T}}$ is a local-level frame gravity vector. It is important to note that these relationships are approximate, since additional errors can integrate into the position and velocity due to gravity model approximations, timing errors, and orientation errors. Even if the biases are perfectly estimated before GNSS becomes unavailable, i.e., $\tilde{\boldsymbol{b}}_{\text{gyr}} = \mathbf{0}_{3\times1}$ and $\tilde{\boldsymbol{b}}_{\text{acc}} = \mathbf{0}_{3\times1}$, the integration of the white noise $\boldsymbol{n}_{\text{gyr}}$ and $\boldsymbol{n}_{\text{acc}}$ will cause the standard deviation of the position error in the ith coordinate direction $\sigma({}^e\tilde{\boldsymbol{r}}_{b,i})$ to grow according to

$$\sigma\left({}^e\tilde{\boldsymbol{r}}_{b,i}\right) = \sqrt{\frac{1}{5}S_{\text{gyr}}t^5}, \quad \sigma\left({}^e\tilde{\boldsymbol{r}}_{b,i}\right) = \sqrt{\frac{1}{3}S_{\text{acc}}t^3}, \quad i = x, y, z$$

respectively, where S_{gyr} and S_{acc} are the one-sided power spectral density (PSD) of $\boldsymbol{n}_{\text{gyr}}$ and $\boldsymbol{n}_{\text{acc}}$, respectively.

From the above relationships, it is obvious that without INS aiding corrections, the position errors and their associated standard deviations grow unboundedly. The next section develops an SOP-aided INS framework, which uses pseudoranges drawn from unknown terrestrial SOPs to provide INS aiding. The following sections demonstrate through simulations and an experiment that the SOP-aided INS reduces ${}^e\tilde{\boldsymbol{r}}_b$ compared to a traditional GNSS-aided INS while GNSS is available and appears to bound ${}^e\tilde{\boldsymbol{r}}_b$ when GNSS becomes unavailable.

IV. SOP-AIDED INERTIAL NAVIGATION

The SOP-aided INS framework provides both accurate and robust navigation with and without GNSS signals by using pseudoranges drawn from ambient terrestrial SOPs to correct INS errors. This section formulates the SOP-aided INS, which operates in two modes.

1) *Mapping Mode*: GNSS pseudoranges are available. Here, GNSS and SOP pseudoranges are fused in the EKF to aid the INS, producing a more accurate estimate of $\boldsymbol{x}_{\text{gnss,ins}}$ while mapping the SOP radio environment (i.e., estimating the unknown states of the SOPs).
2) *Radio SLAM mode*: GNSS pseudoranges are unavailable. Here, SOP pseudoranges aid the INS to simultaneously localize the vehicle-mounted INS (estimate $\boldsymbol{x}_{\text{imu}}$) while mapping the unknown states of the SOPs.

A. SOP Dynamics and Pseudorange Measurement Model

Each of the M SOPs will be assumed to emanate from a spatially stationary terrestrial transmitter. The state vector of the mth SOP $\boldsymbol{x}_{\text{sop},m}$ is defined as $\boldsymbol{x}_{\text{sop},m} \triangleq [{}^{e}\boldsymbol{r}_{\text{sop},m}^{\mathsf{T}}, \boldsymbol{x}_{\text{clk,sop},m}^{\mathsf{T}}]^{\mathsf{T}} \in \mathbb{R}^5$, where ${}^{e}\boldsymbol{r}_{\text{sop},m} \in \mathbb{R}^3$ is its 3D position state and $\boldsymbol{x}_{\text{clk,sop},m} \triangleq [c\delta t_{\text{sop},m}, c\dot{\delta t}_{\text{sop},m}]^{\mathsf{T}} \in \mathbb{R}^2$ is its clock states, where $\delta t_{\text{sop},m}$ and $\dot{\delta t}_{\text{sop},m}$ are the clock bias and drift, respectively. The SOP's discrete-time dynamics are modeled as

$$\boldsymbol{x}_{\text{sop},m}(k+1) = \mathbf{F}_{\text{sop}}\boldsymbol{x}_{\text{sop},m}(k) + \boldsymbol{w}_{\text{sop},m}(k), \quad k = 1, 2, \ldots \tag{10}$$

$$\boldsymbol{x}_{\text{sop},m} = \left[{}^{e}\boldsymbol{r}_{\text{sop},m}^{\mathsf{T}}, \boldsymbol{x}_{\text{clk,sop},m}^{\mathsf{T}}\right]^{\mathsf{T}}, \quad \mathbf{F}_{\text{sop}} = \text{diag}\left[\mathbf{I}_{3\times 3}, \mathbf{F}_{\text{clk}}\right]$$

where $\boldsymbol{w}_{\text{sop},m}$ is the process noise, which is modeled as a discrete-time zero-mean white noise sequence with covariance $\mathbf{Q}_{\text{sop},m} = \text{diag}[\mathbf{0}_{3\times 3}, \mathbf{Q}_{\text{clk,sop},m}]$, with $\mathbf{Q}_{\text{clk,sop},m}$ having identical structure to $\mathbf{Q}_{\text{clk,r}}$ in (7), except that $S_{\tilde{w}_{\delta t_{\text{r}}}}$ and $S_{\tilde{w}_{\dot{\delta t}_{\text{r}}}}$ are replaced with SOP clock-specific spectra $S_{\tilde{w}_{\delta t_{\text{sop},m}}}$ and $S_{\tilde{w}_{\dot{\delta t}_{\text{sop},m}}}$, respectively, where $S_{\tilde{w}_{\delta t_{\text{sop},m}}} \approx \frac{h_{0,\text{sop},m}}{2}$ and $S_{\tilde{w}_{\dot{\delta t}_{\text{sop},m}}} \approx 2\pi^2 h_{-2,\text{sop},m}$.

The pseudorange observation made by the vehicle-mounted receiver on the mth SOP, after discretization and mild approximations discussed in [28], is related to the receiver's and SOP's states by

$$\begin{aligned} z_{\text{sop},m}(j) &= \|{}^{e}\boldsymbol{r}_b(j) - {}^{e}\boldsymbol{r}_{\text{sop},m}\|_2 \\ &\quad + c \cdot \left[\delta t_r(j) - \delta t_{\text{sop},m}(j)\right] + v_{\text{sop},m}(j) \end{aligned} \tag{11}$$

where $v_{\text{sop},m}$ is the measurement noise, which is modeled as a discrete-time zero-mean white Gaussian sequence with variance $\sigma_{\text{sop},m}^2$.

B. Framework Overview

The SOP-aided INS framework illustrated in Fig. 1 operates both with and without GNSS signals. To this end, the framework operates in one of two modes: 1) Mapping mode when GNSS pseudoranges are available and 2) radio SLAM mode when GNSS pseudoranges are unavailable. This subsection describes why special care must be taken when transitioning between GNSS-available and GNSS-unavailable modes and how the transition is performed.

In contrast to a traditional tightly coupled GNSS-aided INS, the SOP-aided INS has the added complexity of having to deal with the unknown, dynamic, and stochastic states of SOPs. These states are estimated simultaneously with $\boldsymbol{x}_{\text{gnss,ins}}$, i.e., the EKF estimates the state vector $\boldsymbol{x} \in \mathbb{R}^{18+5M}$, defined as

$$\boldsymbol{x} \triangleq \left[\boldsymbol{x}_{\text{gnss,ins}}^{\mathsf{T}}, \boldsymbol{x}_{\text{sop},1}^{\mathsf{T}}, \ldots, \boldsymbol{x}_{\text{sop},M}^{\mathsf{T}}\right]^{\mathsf{T}}. \tag{12}$$

Note that the EKF estimates absolute state values instead of state errors, which is another common approach when formulating an EKF for an INS [48]. While GNSS signals are available, $\boldsymbol{x}$ is estimated by the EKF in the mapping mode using the measurement set

$$\boldsymbol{z} = \left[\boldsymbol{z}_{\text{gnss}}^{\mathsf{T}}, \boldsymbol{z}_{\text{sop}}^{\mathsf{T}}\right]^{\mathsf{T}}, \quad \boldsymbol{z}_{\text{gnss}} = \left[z_{\text{gnss},1}, \ldots, z_{\text{gnss},N}\right]^{\mathsf{T}}$$

$$\boldsymbol{z}_{\text{sop}} = \left[z_{\text{sop},1}, \ldots, z_{\text{sop},M}\right]^{\mathsf{T}}.$$

When GNSS signals become unavailable, the measurement set reduces to

$$\boldsymbol{z}' = \boldsymbol{z}_{\text{sop}}.$$

In [29], it was shown that $\boldsymbol{x}$ is stochastically unobservable during GNSS-unavailable modes; specifically, the EKF simultaneously estimating $\boldsymbol{x}_{\text{clk},r}$ and $\boldsymbol{x}_{\text{clk,sop},m}$ using $\boldsymbol{z}'$ produces unbounded clock error estimation uncertainties. For this reason, the SOP-aided INS framework transitions from the mapping mode to the radio SLAM mode, by modifying the state vector to resolve observability issues. Note that the mapping mode is not required as long as the Radio SLAM mode is provided with a prior state estimate; however, it produces correlation between the estimates, which will reduce state estimation errors in the Radio SLAM mode compared to using uncorrelated priors. The transition between the mapping and the radio SLAM modes is developed next to properly initialize the estimates, corresponding estimation uncertainties, and cross-correlations, so that a seamless transition takes place between GNSS-available and GNSS-unavailable modes.

To develop this transition, first note that during the radio SLAM mode, $\boldsymbol{z}_{\text{gnss}}$ is no longer available. Therefore, instead of estimating $\boldsymbol{x}_{\text{clk},r}$ and $\{\boldsymbol{x}_{\text{clk,sop},m}\}_{m=1}^{M}$ individually, the relative clock states between the receiver and each SOP, denoted $\boldsymbol{\Delta}\hat{\boldsymbol{x}}_{\text{clk},m} \triangleq \boldsymbol{x}_{\text{clk,r}} - \boldsymbol{x}_{\text{clk,sop},m}$, $m = 1, 2, \ldots, M$, will be estimated. As such, the state vector to be estimated is modified from (12) to become

$$\boldsymbol{x}' = \left[\boldsymbol{x}_{\text{imu}}^{\mathsf{T}}, {\boldsymbol{x}'_{\text{sop},1}}^{\mathsf{T}}, \ldots, {\boldsymbol{x}'_{\text{sop},M}}^{\mathsf{T}}\right]^{\mathsf{T}} \tag{13}$$

where $\boldsymbol{x}'_{\text{sop},m} \triangleq [{}^{e}\boldsymbol{r}^{\mathsf{T}}_{\text{sop},m},\ \boldsymbol{\Delta x}^{\mathsf{T}}_{\text{clk},m}]^{\mathsf{T}}, m = 1, 2, \ldots, M$. At the moment of transition from GNSS-available to GNSS-unavailable, an estimate of the new state vector $\boldsymbol{x}'$ and the corresponding estimation error covariance $\mathbf{P}'$ are initialized from the latest produced estimate $\hat{\boldsymbol{x}}$ and its corresponding estimation error covariance $\mathbf{P}$ using

$$\hat{\boldsymbol{x}}' = \mathbf{T}\hat{\boldsymbol{x}}, \qquad \mathbf{P}' = \mathbf{MPM}^{\mathsf{T}}$$

$$\mathbf{T} = \begin{bmatrix} \mathbf{T}_{\text{gnss,ins}} & \mathbf{0}_{16\times5} & \cdots & \mathbf{0}_{16\times5} \\ \mathbf{T}_{\text{clk,r}} & \mathbf{T}_{\text{sop}} & \cdots & \mathbf{0}_{5\times5} \\ \vdots & \vdots & \ddots & \vdots \\ \mathbf{T}_{\text{clk,r}} & \mathbf{0}_{5\times5} & \cdots & \mathbf{T}_{\text{sop}} \end{bmatrix}$$

$$\mathbf{M} = \begin{bmatrix} \mathbf{M}_{\text{gnss,ins}} & \mathbf{0}_{15\times5} & \cdots & \mathbf{0}_{15\times5} \\ \mathbf{M}_{\text{clk,r}} & \mathbf{T}_{\text{sop}} & \cdots & \mathbf{0}_{5\times5} \\ \vdots & \vdots & \ddots & \vdots \\ \mathbf{M}_{\text{clk,r}} & \mathbf{0}_{5\times5} & \cdots & \mathbf{T}_{\text{sop}} \end{bmatrix}$$

$$\mathbf{T}_{\text{gnss,ins}} \triangleq \left[\mathbf{I}_{16\times16},\ \mathbf{0}_{16\times2}\right], \quad \mathbf{T}_{\text{clk,r}} \triangleq \begin{bmatrix} \mathbf{0}_{3\times16} & \mathbf{0}_{3\times2} \\ \mathbf{0}_{2\times16} & \mathbf{I}_{2\times2} \end{bmatrix}$$

$$\mathbf{T}_{\text{sop}} \triangleq \begin{bmatrix} \mathbf{I}_{3\times3} & \mathbf{0}_{3\times2} \\ \mathbf{0}_{2\times3} & -\mathbf{I}_{2\times2} \end{bmatrix}$$

$$\mathbf{M}_{\text{gnss,ins}} \triangleq \left[\mathbf{I}_{15\times15},\ \mathbf{0}_{15\times2}\right],$$

$$\mathbf{M}_{\text{clk,r}} \triangleq \begin{bmatrix} \mathbf{0}_{3\times15} & \mathbf{0}_{3\times2} \\ \mathbf{0}_{2\times15} & \mathbf{I}_{2\times2} \end{bmatrix}.$$

Notice that $\mathbf{P}$ and $\mathbf{P}'$ has one less dimension than $\hat{\boldsymbol{x}}$ and $\hat{\boldsymbol{x}}'$, respectively. This is due to the IMU's orientation estimation error being represented by a three-axis error angle vector, denoted by $\tilde{\boldsymbol{\theta}} \in \mathbb{R}^3$, which has one less dimension than the estimate of ${}^{b}_{e}\bar{\boldsymbol{q}}$, denoted ${}^{b}_{e}\hat{\bar{\boldsymbol{q}}} \in \mathbb{R}^4$. The vector $\tilde{\boldsymbol{\theta}}$ is related to ${}^{b}_{e}\bar{\boldsymbol{q}}$, and ${}^{b}_{e}\hat{\bar{\boldsymbol{q}}}$ through

$$ {}^{b}_{e}\bar{\boldsymbol{q}} = {}^{b}_{e}\hat{\bar{\boldsymbol{q}}} \otimes \tilde{\bar{\boldsymbol{q}}}, \quad \tilde{\bar{\boldsymbol{q}}} = \left[\frac{1}{2}\tilde{\boldsymbol{\theta}}^{\mathsf{T}},\ \sqrt{1 - \frac{1}{4}\tilde{\boldsymbol{\theta}}^{\mathsf{T}}\tilde{\boldsymbol{\theta}}} \right]^{\mathsf{T}} \tag{14}$$

where $\otimes$ denotes quaternion product. This error representation is common when estimating quaternions, since $\tilde{\bar{\boldsymbol{q}}}$ is an overdetermined representation of the orientation error. Hence, the estimation error covariance associated with $\tilde{\bar{\boldsymbol{q}}}$ would be singular. To avoid singularity, the covariance associated with $\tilde{\boldsymbol{\theta}}$ is maintained instead.

To summarize, the two modes of operation are as follows.

1) *Mapping Mode*: Estimates $\boldsymbol{x}$ using the measurement set $\boldsymbol{z}$.
2) *Radio SLAM Mode*: Estimates $\boldsymbol{x}'$ using the measurement set $\boldsymbol{z}'$.

The EKF time and measurement updates are provided next.

C. EKF Time Update

The time update should be adjusted according to the current operation mode to account for the state transformation from (12) to (13).

1) *Time Update Equations for Mapping Mode:* During the mapping mode, the EKF produces the time update estimate of $\boldsymbol{x}(k+1)$, denoted by $\hat{\boldsymbol{x}}(k+1|j) \triangleq \mathbb{E}[\boldsymbol{x}(k+1)|\{\boldsymbol{z}(i)\}_{i=1}^{j}]$, and an associated prediction error covariance $\mathbf{P}(k+1|j)$, where $k \geq j$, and j is the last time-step an INS-aiding source was available. The time update equations for each component of (12) are provided next. The time update of $\boldsymbol{x}_{\text{imu}}$ is produced using $\boldsymbol{z}_{\text{imu}}$ through the INS illustrated in Fig. 3. The discrete-time linearized equations to produce the one-step time update $\hat{\boldsymbol{x}}_{\text{imu}}$ are provided in Appendix A. The receiver's one-step clock state time update follows from (6) and is given by

$$\hat{\boldsymbol{x}}_{\text{clk,r}}(k+1|j) = \mathbf{F}_{\text{clk}}\hat{\boldsymbol{x}}_{\text{clk,r}}(k|j). \tag{15}$$

The SOPs' one-step state time update follows from (10) and is given by

$$\hat{\boldsymbol{x}}_{\text{sop},m}\left(k+1|j\right) = \mathbf{F}_{\text{sop}}\hat{\boldsymbol{x}}_{\text{sop},m}(k|j), \quad m = 1, \ldots, M. \tag{16}$$

Next, the one-step prediction error covariance is produced according to

$$\begin{aligned} &\mathbf{P}(k+1|j) = \mathbf{F}(k)\mathbf{P}(k|j)\mathbf{F}^{\mathsf{T}}(k) + \mathbf{Q}(k) \\ &\mathbf{F}(k) \triangleq \text{diag}\left[\boldsymbol{\Phi}_{\text{imu}}(k+1,k),\ \mathbf{F}_{\text{clk}},\ \mathbf{F}_{\text{sop}},\ \ldots,\ \mathbf{F}_{\text{sop}}\right] \\ &\mathbf{Q}(k) \triangleq \text{diag}\left[\mathbf{Q}_{\text{imu}}(k),\ \mathbf{Q}_{\text{clk},r},\ \mathbf{Q}_{\text{sop}},\ \ldots,\ \mathbf{Q}_{\text{sop}}\right] \end{aligned} \tag{17}$$

where $\boldsymbol{\Phi}_{\text{imu}}$ and $\mathbf{Q}_{\text{imu}}$ are the discrete-time linearized INS state transition matrix and process noise covariance, respectively, which are provided in Appendix B.

2) *Time Update Equations for Radio SLAM Mode:* During the radio SLAM mode, the state time update has the same form as the mapping mode, except that (15) is omitted and the SOP state time update (16) is replaced with the SOP position and relative clock state time update, which is given by

$$\hat{\boldsymbol{x}}'_{\text{sop},m}\left(k+1|j\right) = \mathbf{F}_{\text{sop}}\hat{\boldsymbol{x}}'_{\text{sop},m}(k|j), \quad m = 1, \ldots, M.$$

The prediction error covariance $\mathbf{P}'(k+1|j)$ has the same form as (17), except that $\mathbf{F}$ is replaced with $\mathbf{F}' \triangleq \text{diag}[\boldsymbol{\Phi}_{\text{imu}},\ \mathbf{F}_{\text{sop}},\ \ldots,\ \mathbf{F}_{\text{sop}}]$ and $\mathbf{Q}$ is replaced with $\mathbf{Q}' \triangleq \mathbf{MQM}^{\mathsf{T}}$.

D. EKF Measurement Update

The measurement update should be adjusted according to the current operation mode to account for the change of measurement availability from $\boldsymbol{z}$ to $\boldsymbol{z}'$.

1) *Measurement Update Equations for Mapping Mode:* Assuming $\boldsymbol{z}(k+1)$ is available, the EKF measurement update step will produce $\hat{\boldsymbol{x}}(k+1|k+1)$. The standard EKF measurement update equations are slightly modified to map the 3D orientation error correction to the 4D quaternion state estimate. To avoid convoluting this section, the full set of EKF state measurement update equations to produce $\hat{\boldsymbol{x}}(k+1|k+1)$ are provided in Appendix C. Given a prediction error covariance $\mathbf{P}(k+1|j)$, the corresponding corrected error covariance is given by

$$\begin{aligned} &\mathbf{P}(k{+}1|k{+}1) = \mathbf{P}(k{+}1|j) - \mathbf{K}(k{+}1)\mathbf{S}(k{+}1)\mathbf{K}^{\mathsf{T}}(k{+}1) \\ &\mathbf{K}(k{+}1) \triangleq \mathbf{P}(k{+}1|j)\mathbf{H}^{\mathsf{T}}(k{+}1)\mathbf{S}^{-1}(k{+}1) \end{aligned} \tag{18}$$

$$\mathbf{S}(k+1) \triangleq \mathbf{H}(k+1)\mathbf{P}(k+1)\mathbf{H}^{\mathsf{T}}(k+1) + \mathbf{R}(k+1) \tag{19}$$

where $\mathbf{H}$ is the measurement Jacobian and $\mathbf{R}$ is the measurement noise covariance of z. In the mapping mode, i.e., $z \triangleq [z_{\text{gnss}}^{\mathsf{T}}, z_{\text{sop}}^{\mathsf{T}}]^{\mathsf{T}}$, the measurement Jacobian $\mathbf{H}$ is

$$\mathbf{H} = \left[\mathbf{H}_{\text{gnss}}^{\mathsf{T}},\ \mathbf{H}_{\text{sop}}^{\mathsf{T}}\right]^{\mathsf{T}}$$

$$\mathbf{H}_{\text{gnss}} = \begin{bmatrix} \mathbf{0}_{1\times 3} & \hat{\boldsymbol{l}}_{\text{gnss},1}^{\mathsf{T}} & \mathbf{0}_{1\times 9} & \boldsymbol{h}_{\text{clk}}^{\mathsf{T}} & \mathbf{0}_{1\times 5\,M} \\ \vdots & \vdots & \vdots & \vdots & \vdots \\ \mathbf{0}_{1\times 3} & \hat{\boldsymbol{l}}_{\text{gnss},N}^{\mathsf{T}} & \mathbf{0}_{1\times 9} & \boldsymbol{h}_{\text{clk}}^{\mathsf{T}} & \mathbf{0}_{1\times 5\,M} \end{bmatrix}$$

$$\mathbf{H}_{\text{sop}} = \begin{bmatrix} \mathbf{0}_{1\times 3} & \hat{\boldsymbol{l}}_{\text{sop},1}^{\mathsf{T}} & \mathbf{0}_{1\times 9} & \boldsymbol{h}_{\text{clk}}^{\mathsf{T}} & \hat{\boldsymbol{h}}_{\text{sop},1}^{\mathsf{T}} & \cdots & \mathbf{0} \\ \vdots & \vdots & \vdots & \vdots & \vdots & \ddots & \vdots \\ \mathbf{0}_{1\times 3} & \hat{\boldsymbol{l}}_{\text{sop},M}^{\mathsf{T}} & \mathbf{0}_{1\times 9} & \boldsymbol{h}_{\text{clk}}^{\mathsf{T}} & \mathbf{0} & \cdots & \hat{\boldsymbol{h}}_{\text{sop},M}^{\mathsf{T}} \end{bmatrix}$$

where $\hat{\boldsymbol{l}}_{\text{gnss},n} \triangleq \frac{{}^e\hat{\boldsymbol{r}}_b - {}^e\boldsymbol{r}_{\text{gnss},n}}{\|{}^e\hat{\boldsymbol{r}}_b - {}^e\boldsymbol{r}_{\text{gnss},n}\|}$, $\boldsymbol{h}_{\text{clk}} \triangleq [1,\ 0]^{\mathsf{T}}$, $\hat{\boldsymbol{l}}_{\text{sop},m} \triangleq \frac{{}^e\hat{\boldsymbol{r}}_b - {}^e\hat{\boldsymbol{r}}_{\text{sop},m}}{\|{}^e\hat{\boldsymbol{r}}_b - {}^e\hat{\boldsymbol{r}}_{\text{sop},m}\|}$, and $\boldsymbol{h}_{\text{sop},m} \triangleq [-\hat{\boldsymbol{l}}_{\text{sop},m}^{\mathsf{T}},\ -\boldsymbol{h}_{\text{clk}}^{\mathsf{T}}]^{\mathsf{T}}$.

2) *Measurement Update Equations for Radio SLAM Mode:* During the radio SLAM mode, the state and covariance update equations have the same form, except the measurement Jacobian is adjusted from $\mathbf{H}$ to $\mathbf{H}'$ to account for only SOP pseudoranges being available, i.e., $z' = z_{\text{sop}}$ and $\mathbf{R}$ is replaced with $\mathbf{R}'$, which is the measurement noise covariance of z'. The adjusted measurement Jacobian is

$$\mathbf{H}' = \begin{bmatrix} \mathbf{0}_{1\times 3} & \hat{\boldsymbol{l}}_{\text{sop},1}^{\mathsf{T}} & \mathbf{0}_{1\times 9} & \boldsymbol{v}_{\text{sop},1}^{\mathsf{T}} & \cdots & \mathbf{0} \\ \vdots & \vdots & \vdots & \vdots & \ddots & \vdots \\ \mathbf{0}_{1\times 3} & \hat{\boldsymbol{l}}_{\text{sop},M}^{\mathsf{T}} & \mathbf{0}_{1\times 9} & \mathbf{0} & \cdots & \boldsymbol{v}_{\text{sop},M}^{\mathsf{T}} \end{bmatrix}$$

where $\boldsymbol{v}_{\text{sop},m} \triangleq [-\hat{\boldsymbol{l}}_{\text{sop},m}^{\mathsf{T}},\ \boldsymbol{h}_{\text{clk}}^{\mathsf{T}}]^{\mathsf{T}}$.

V. SIMULATION STUDY

This section presents simulation results demonstrating a UAV navigating via the tightly coupled SOP-aided INS framework developed in Section IV. The SOP-aided INS is first compared against a traditional tightly coupled GNSS-aided INS. Then, the performance is studied by varying the quantity and quality of exploited terrestrial SOPs.

A. Numerical Simulator Description

A numerical simulator was developed to generate the following.

1) *"Ground Truth" Trajectory of the UAV*: The trajectory was generated using a six degrees-of-freedom (6DoF) kinematic model [48], which included a straight segment with linear acceleration, a 5° pitching climb, a straight segment without acceleration, and four 60° banking turns, performed over a 200-s period. During the first 100 s of the trajectory, the UAV completes all maneuvers except for the last three banking turns, which are then completed during the remaining 100 s. This particular trajectory was chosen because it excites all 6DoF of the UAV, i.e., both horizontal and vertical directions and all three angles (roll, pitch, and yaw), allowing the SOP-aided INS to be studied under various maneuvers. The trajectory that the UAV traversed is illustrated in Fig. 4.

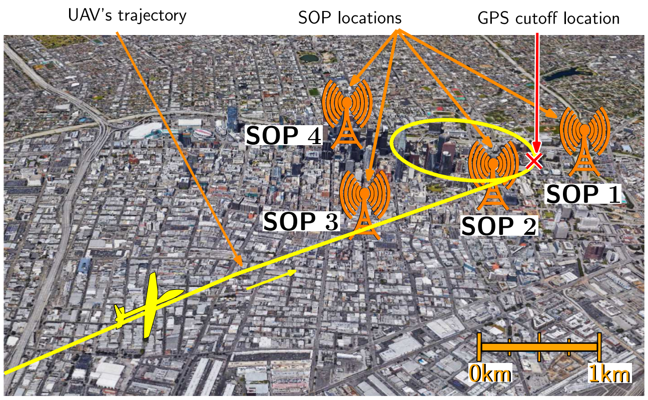

Fig. 4. True trajectory the UAV traversed (yellow) and SOP locations (orange transmitters). The GPS cutoff location is marked with X.

TABLE I
INS Process Noise Covariances

	Consumer	Tactical
$\mathbf{Q}_{\boldsymbol{n}_{\text{gyr}}}$ [rad^2/sec^2]	$2.74\cdot(10^{-4})\cdot\mathbf{I}_{3\times 3}$	$3.38\cdot(10^{-9})\cdot\mathbf{I}_{3\times 3}$
$\mathbf{Q}_{\boldsymbol{n}_{\text{acc}}}$ [m^2/sec^4]	$6.01\cdot(10^{-4})\cdot\mathbf{I}_{3\times 3}$	$3.38\cdot(10^{-9})\cdot\mathbf{I}_{3\times 3}$
$\mathbf{Q}_{\boldsymbol{w}_{\text{gyr}}}$ [rad^2/sec^2]	$(10^{-10})\cdot\mathbf{I}_{3\times 3}$	$(10^{-14})\cdot\mathbf{I}_{3\times 3}$
$\mathbf{Q}_{\boldsymbol{w}_{\text{acc}}}$ [m^2/sec^4]	$(10^{-10})\cdot\mathbf{I}_{3\times 3}$	$(10^{-14})\cdot\mathbf{I}_{3\times 3}$

2) *Gyroscope and Accelerometer Data*: These data were generated at 100 Hz according to (1) and (2), respectively, for a tactical-grade and a consumer-grade IMU. The random noise for each of the axes of the tactical-grade IMU was set to have a PSD of 10 deg $/\sqrt{\text{hr}}$ and 1000 μg$/\sqrt{\text{Hz}}$ for the gyroscope and accelerometer, respectively. The random noise for consumer-grade IMUs are typically stated in terms of total accumulated noise at the output of the sensor. Each axis of the consumer-grade IMU was set to have an accumulated noise of 0.3 deg /s and 2.5 mg for the gyroscope and accelerometer, respectively. The evolution of the biases were generated according to (3) and (4) using driving process noise with spectra set to $\mathbf{S}_{\boldsymbol{w}_{\text{gyr}}} \equiv 10^{-8} \cdot \mathbf{I}_{3\times 3}$ and $\mathbf{S}_{\boldsymbol{w}_{\text{acc}}} \equiv 10^{-8} \cdot \mathbf{I}_{3\times 3}$, for consumer grade and $\mathbf{S}_{\boldsymbol{w}_{\text{gyr}}} \equiv 10^{-12} \cdot \mathbf{I}_{3\times 3}$ and $\mathbf{S}_{\boldsymbol{w}_{\text{acc}}} \equiv 10^{-12} \cdot \mathbf{I}_{3\times 3}$ for tactical-grade, respectively. These spectra are mapped online to the discrete-time noise covariances $\mathbf{Q}_{\boldsymbol{n}_{\text{gyr}}}$, $\mathbf{Q}_{\boldsymbol{n}_{\text{acc}}}$, $\mathbf{Q}_{\boldsymbol{w}_{\text{gyr}}}$, and $\mathbf{Q}_{\boldsymbol{w}_{\text{acc}}}$ through the equations provided in Appendix B. The resulting covariance matrices for both the tactical and consumer-grade IMU used in this simulation are listed in Table I.

TABLE II
GPS and SOP Measurement Noise Standard Deviations

	Minimum [m]	**Mean [m]**	**Maximum [m]**
GPS	2.79	3.24	3.51
SOP	0.859	1.69	3.53

3) *GPS L1 C/A Pseudoranges*: These pseudoranges were generated at 1 Hz according to (9), using satellite orbits produced from receiver independent exchange (RINEX) files downloaded from a continuously operating reference station (CORS) server [53]. The GPS pseudorange measurement noise $\{v_{\text{gnss},n}(j)\}_{n=1}^{N}$ were set to be independent with a measurement noise variance computed according to [54]

$$\sigma^2_{\text{gnss},n,j} = \frac{c^2 t_{\text{eml}} B_{\text{DLL}} T_c^2 \sigma_s^2}{2(C/N_0)_{n,j}}\left[1+\frac{1}{T_{\text{CO}}(C/N_0)_{n,j}}\right] \quad (20)$$

where $t_{\text{eml}} \equiv 0.5$ chips is the early-minus-late correlator spacing, $B_{\text{DLL}} \equiv 0.05$ Hz is the delay lock loop (DLL) bandwidth, $T_c \equiv 1/(1.023 \times 10^6)$ s is the chip duration, $(C/N_0)_{n,j}$ (in Hz) is the time-varying received carrier-to-noise ratio, which was derived from the RINEX files, $\sigma_s \equiv 17$ is a scaling parameter to account for unmodeled errors, and $T_{CO} \equiv 10$ ms is the coherent integration time. Another common model often employed is the scaled C/N_0 - elevation model [55]. The minimum, mean, and maximum measurement noise standard deviation across all GPS satellites over the simulation time from using (20) are tabulated in Table II. The receiver was set to be equipped with a typical temperature-compensated crystal oscillator (TCXO), with values specified in Table V.

4) *SOP Pseudoranges*: These pseudoranges were generated at 5 Hz according to (11). The SOP pseudorange measurement noise $\{v_{\text{sop},m}(j)\}_{m=1}^{M}$ were set to be independent with a time-varying measurement noise variance which corresponds to code division multiple access (CDMA) signals, computed according to (20), except that $t_{\text{eml}} \equiv 1$, $\sigma^2_{\text{gnss},n,j}$ is replaced with $\sigma^2_{\text{sop},m,j}$, $T_c \equiv 1/(1.2288 \times 10^6)$, $\sigma_s \equiv 22$, $T_{CO} \equiv 1/37.5$ s, and the carrier-to-noise ratio $(C/N_0)_{n,j}$ is replaced with a time-varying log-distance path loss model [56]

$$(C/N_0)'_{m,j} = P_0 - 10\gamma \cdot \log_{10}(d(j)/D_0)$$
$$(C/N_0)_{m,j} = 10^{[(C/N_0)'_{m,j}/10]}$$

where $P_0 \equiv 56$ dB-Hz is a calibration carrier-to-noise ratio at a distance $D_0 \equiv 1400$ m, $d(j) \triangleq \|{}^e\boldsymbol{r}_b(j) - {}^e\boldsymbol{r}_{\text{sop},m}\|_2$, and $\gamma \equiv 2$ is the path loss exponent. The calibration values P_0 and D_0 are values commonly observed by the authors during experimental campaigns [14]. The SOP pseudorange measurement noise variance computation assumes that the correlation function within the DLL is equivalent to GPS. This is a reasonable assumption for cellular CDMA signals when t_{eml} is between 0.8 and 1.25 chips. More sophisticated models are discussed in [57]. The minimum, mean, and maximum measurement noise standard deviation across all SOPs over the simulation time are tabulated in Table II. The SOP dynamics evolved according to (10). Each SOP was set to be equipped with a typical oven-controlled crystal oscillator (OCXO), with values specified in Table V. The SOP transmitters' positions $\{{}^e\boldsymbol{r}_{\text{sop},m}\}_{m=1}^{4}$ were surveyed from cellular tower locations in downtown Los Angeles, California, USA.

B. Simulation Results: Tightly Coupled SOP-Aided INS Versus GNSS-Aided INS

To study the navigation performance of the tightly coupled SOP-aided INS, it is compared against a tightly coupled GNSS-aided INS during GNSS-available and GNSS-unavailable modes. The SOP-aided INS framework was assumed to be equipped with a consumer-grade IMU, while the GNSS-aided INS framework was assumed to be equipped with a tactical-grade IMU. For both frameworks, GPS pseudoranges were set to be available for $t \in [0100)$ s and unavailable for $t \in [100, 200]$ s. During the first 100 s, the inertial radio SLAM framework is in the mapping mode, which causes the estate estimates to begin to converge. This will be illustrated later in the results. The initial estimates (at $t = 0$ s) of the UAV's states were initialized with a random error drawn according to $\tilde{\boldsymbol{x}}_{\text{gnss,ins}}(0|0) \sim \mathcal{N}[\mathbf{0}_{17\times1},\ \mathbf{P}_{\boldsymbol{x}_{\text{gnss,ins}}}(0|0)]$, where

$$\mathbf{P}_{\boldsymbol{x}_{\text{gnss,ins}}}(0|0) \triangleq \text{diag}\left[\mathbf{P}_{\boldsymbol{x}_{\text{imu}}}(0|0),\ \mathbf{P}_{\boldsymbol{x}_{\text{clk,r}}}(0|0)\right]$$
$$\mathbf{P}_{\boldsymbol{x}_{\text{imu}}}(0|0) \equiv \text{diag}\left[(10^{-2})\cdot\mathbf{I}_{3\times3},\ 9\cdot\mathbf{I}_{3\times3},\ \mathbf{I}_{3\times3},\ (10^{-4})\cdot\mathbf{I}_{6\times6}\right]$$
$$\mathbf{P}_{\boldsymbol{x}_{\text{clk,r}}}(0|0) \equiv \text{diag}\,[9,\ 1]\,.$$

For the SOP-aided INS framework, the SOPs' state estimates were initialized according to $\hat{\boldsymbol{x}}_{\text{sop},m}(0|0) \sim \mathcal{N}[\boldsymbol{x}_{\text{sop},m}(0), \mathbf{P}_{\text{sop}}(0|0)]$, for $m = 1, \ldots, M$, where $\boldsymbol{x}_{\text{sop},m}(0) \equiv [{}^e\boldsymbol{r}^{\mathsf{T}}_{\text{sop},m},\ 10^4,\ 10]^{\mathsf{T}}$, $\mathbf{P}_{\text{sop}}(0|0) \equiv (10^4)\cdot \text{diag}[\mathbf{I}_{3\times3},\ 0.1,\ 0.01]$. Note that the estimate of the SOPs' states are initialized by drawing from a Gaussian distribution with a mean equal to the true states and a covariance to capture uncertainty. This initialization scheme is used in simulation to ensure consistent initial priors in the EKF. In practice, if the initial SOPs' states are completely unknown, then a small time history of pseudoranges from the beginning of the run can be saved and processed through a batch filter to estimate these states. Then, the estimate and associated covariance of the batch filter can be used to initialize the EKF. As long as the vehicle is moving and has access to GPS, the position and clock states of the SOPs are observable [28], [29]. The simulated trajectory, SOP positions, the GPS cutoff location are illustrated in Fig. 4. The GPS and SOP pseudorange measurement noise standard deviations used in the EKF were set to the same time-varying values that were used

TABLE III
SOP Final Error and RMSD

	SOP 1	SOP 2	SOP 3	SOP 4
Final error [m]	2.117	2.077	0.623	0.776
Final RMSD [m]	3.435	2.823	1.599	3.823

to generate the measurements, which are discussed in Section V-A.

Before the simulation results are presented, it is worth discussing the feasibility of the simulation scenario illustrated in Fig. 4 with two remarks.

REMARK 1 Notice that at some points during the UAV's trajectory, some of the SOPs are around 5 km from the UAV and have overlapping coverage areas with each other. In practice, towers typically transmit in all directions from three sets of antennas that are spaced 120 degrees apart. Since SOP navigation receivers are not subscribers to the network (e.g., as a cell phone user is), the receiver is not limited to the artificial coverage areas that service provider user equipment impose to ensure that the device has optimal reception. A universal software radio peripheral (USRP) mounted to a vehicle can certainly sample and receive powerful signals from overlapping coverage areas, especially if they are flying in the air over the buildings. During several experiments conducted by the authors, signals from 10 *independent* towers were received simultaneously, some of which were more than 6 km away [38]. The signals had a received carrier-to-noise ratio greater than 35 dB-Hz for 8 of the towers and greater than 27 dB-Hz for the other two, which was high enough to produce useful pseudoranges to all 10 towers.

REMARK 2 The UAV trajectory may cross from one sector to another of the same tower. Crossing sectors of the same tower would introduce a shift in the observed clock bias due to an offset in the pseudorandom noise (PN) sequence and other effects, such as unmodeled distance between the phase-center of the sector antennas and delays due to RF components (e.g., connectors, cabling, filters, amplifiers, etc.). This behavior was *not* simulated and only a single aggregated SOP position was used to simulate pseudoranges from each tower. In practice, when the UAV transitions from one sector to another, the clock shift due to the PN sequence offset should be removed from the clock bias estimate in the EKF. After removing this shift, the remaining shift can be modeled as a stochastic process that follows an autoregressive (AR) model. This behavior and the characterization of the AR model is detailed in [57].

The resulting estimation error trajectories and corresponding ±three-standard deviation bounds ($\pm 3\sigma$) for the position of the UAV and SOP 1 are plotted in Figs. 5 and 6, respectively. The final 3D position error and root mean squared deviation (RMSD) for SOPs 1–4 are tabulated in Table III. The RMSD is defined as

$$\text{RMSD} \triangleq \sqrt{\text{Tr}\left[\mathbf{P}_{{}^e\boldsymbol{r}_{\text{sop},m}}\right]}$$

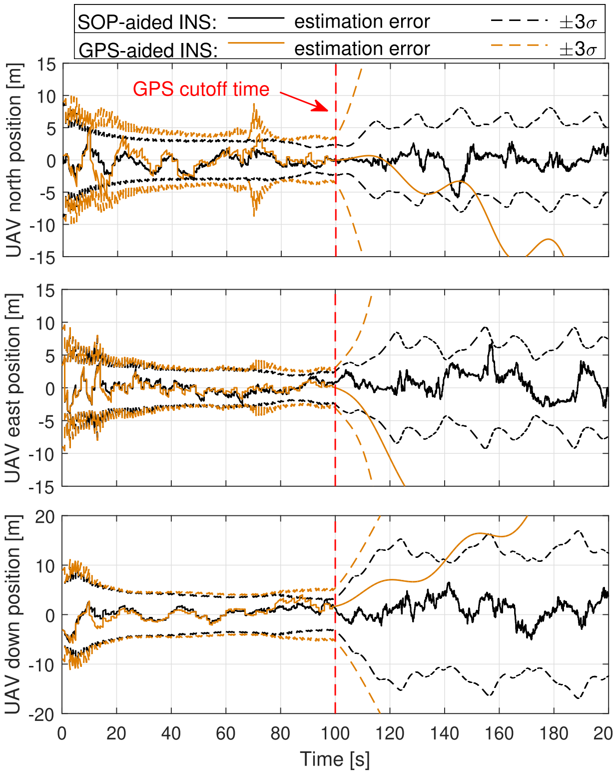

Fig. 5. Tesulting north, east, and down position errors for the UAV are illustrated for two frameworks. In both frameworks, the UAV had access to GPS pseudoranges for only the first 100 s while traversing the trajectory illustrated in Fig. 4, after which GPS pseudoranges were cut off. The GPS cutoff time is marked with a red dashed vertical line. The first framework used a tightly-coupled GPS-aided INS with a tactical-grade IMU (orange). In the second framework used an SOP-aided INS (black).

where $\text{Tr}[\mathbf{A}]$ is the trace of matrix $\mathbf{A}$ and $\mathbf{P}_{{}^e\boldsymbol{r}_{\text{sop},m}}$ is the covariance of the mth SOP's position estimate.

The following may be concluded from Figs. 5 and 6. First, when GPS pseudoranges became unavailable at $t = 100$ s, the UAV's north, east, and down estimation error variances associated with the traditional GPS-aided INS begin to diverge unboundedly, as expected, whereas the errors associated with the SOP-aided INS appear bounded. Second, before GPS cutoff, the SOP-aided INS with a *consumer-grade* IMU yielded lower estimation error variances when compared to the traditional GPS-aided INS with a *tactical-grade* IMU; therefore, including SOP pseudoranges along with GPS pseudoranges to aid an INS may relax requirements on IMU quality. The benefits of including SOP pseudoranges along with GPS pseudoranges are partly attributed to improved pseudorange geometric diversity. This diversity produces smaller estimation errors due to a reduced geometric dilution of precision (GDOP), horizontal dilution of precision (HDOP), and VDOP, as can be seen by comparing the values for using GPS only and GPS+SOPs, tabulated in Table IV. Third, the SOPs' north, east, and down estimation error variances suddenly reduce at approximately 65 s due to the UAV's left banking turn, causing a rapid change in the angle of the line-of-sight vector from

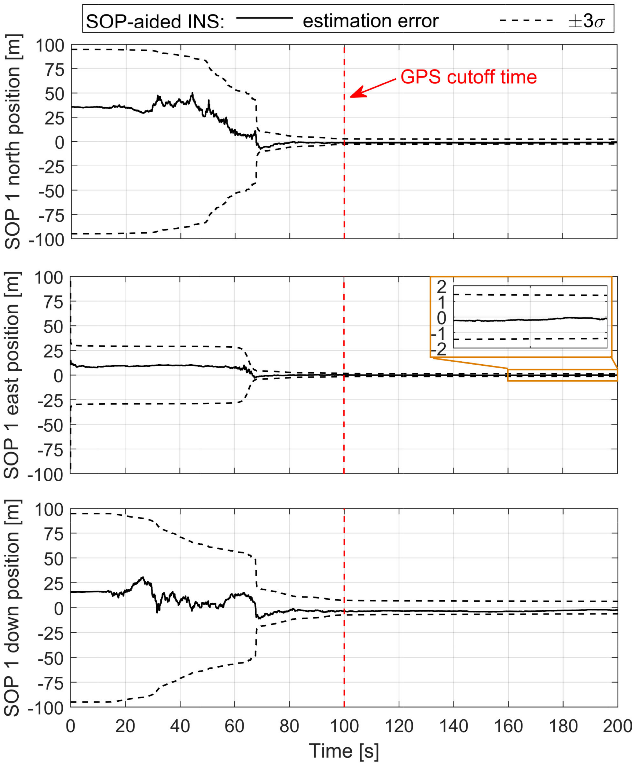

Fig. 6. Resulting north, east, and down position errors and corresponding $\pm 3\sigma$ bounds (black) for SOP 1. The GPS cutoff time is marked with a red dashed vertical line.

TABLE IV
Minimum and Maximum GDOP, HDOP, and VDOP

	GPS only	**GPS+SOPs**
Minimum GDOP	1.928	0.927
Maximum GDOP	1.934	1.027
Minimum HDOP	1.027	0.695
Maximum HDOP	1.030	0.902
Minimum VDOP	1.358	0.514
Maximum VDOP	1.362	0.609

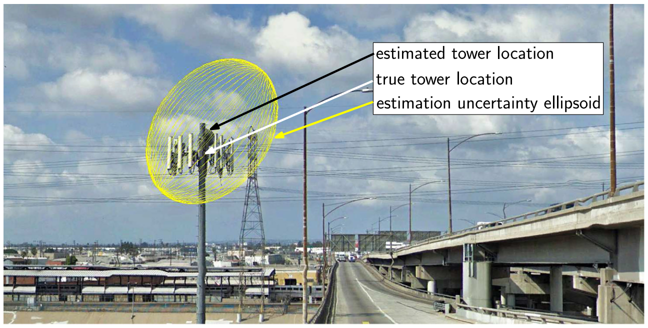

Fig. 7. True position, final position estimate, and final 99th–percentile uncertainty ellipsoid for SOP 1.

the UAV to the SOP, which improves the estimability of the SOP's position. The uncertainty continues to reduce after GPS is cut off, indicating the SOPs' position states are stochastically observable in the radio SLAM mode. Fourth, the SOPs' position errors are consistent with the $\pm 3\sigma$ bounds, i.e., the produced error variances are correctly representing the estimation uncertainty. This can be seen visually in Fig. 7, which illustrates that the true position of SOP 1 is contained within the final 99th–percentile uncertainty ellipsoid, which is centered at the final estimated position. Similar behavior was observed for SOPs 2, 3, and 4 and after simulation runs using different realizations of process noise and measurement noise.

During these simulations it was assumed that pseudorange measurements from all four SOPs were available at 5 Hz, without interruption. If at any point in time pseudoranges become faulty from any of the SOPs, then the fault can be detected and the pseudoranges associated with that SOP should be temporarily excluded using a receiver autonomous integrity monitoring (RAIM) framework for SOPs [58]. The UAV's position errors and associated estimation uncertainty will increase when an SOP is excluded, since less measurements are available. The degradation in performance due to excluding a varying number of SOP's pseudoranges is studied in the next subsection.

The plots in Fig. 8(a)–(b) correspond to the estimation errors of the receiver's clock bias $c\delta t_{\text{r}}$ and clock drift $c\dot{\delta t}_{\text{r}}$, respectively, when GPS was available and the plots in Fig. 8(c)–(d) correspond to the estimation errors of SOP 1's clock bias $c\delta t_{\text{sop},1}$ and clock drift $c\dot{\delta t}_{\text{sop},1}$, respectively, while GPS was available. Fig. 8(e)–(f) correspond to the estimation errors of the relative bias $c\Delta\delta t_1$ and drift $c\Delta\dot{\delta t}_1$ between the UAV-mounted receiver and SOP 1 that were initialized when GPS pseudoranges became unavailable, as was described in Section IV-B. Note from Fig. 8(a)–(b) that including SOP pseudoranges along with GPS pseudoranges reduces the estimation uncertainty associated with $c\delta t_{\text{r}}$ and $c\dot{\delta t}_{\text{r}}$ compared to using GPS pseudoranges alone. Also note from Fig. 8(e)–(f), that the initialization scheme discussed in Section IV-B produces consistent estimates of $c\Delta\delta t_1$ and drift $c\Delta\dot{\delta t}_1$ the moment GPS gets cut off and that these states are estimable during the GPS cutoff period. Similar behavior has been observed through extensive experimental campaigns conducted by the authors [43], [44], [59]. In contrast, if $c\delta t_{\text{r}}$, $c\dot{\delta t}_{\text{r}}$, and $c\delta t_{\text{sop},1}$, $c\dot{\delta t}_{\text{sop},1}$ were estimated individually, their estimation errors would have diverged unboundedly [29].

C. Performance Analysis

Several factors affect the navigation performance when exploiting SOP pseudoranges to aid an INS. The main factors are: Quantity of SOPs, quality of SOP-equipped oscillators, quality of receiver-equipped oscillator, receiver-to-SOP geometry, channel (e.g., line of sight conditions and multipath), and outliers due to unmodeled effects. In what follows, the performance sensitivity of the SOP-aided INS is studied by varying the quantity of SOPs and quality of

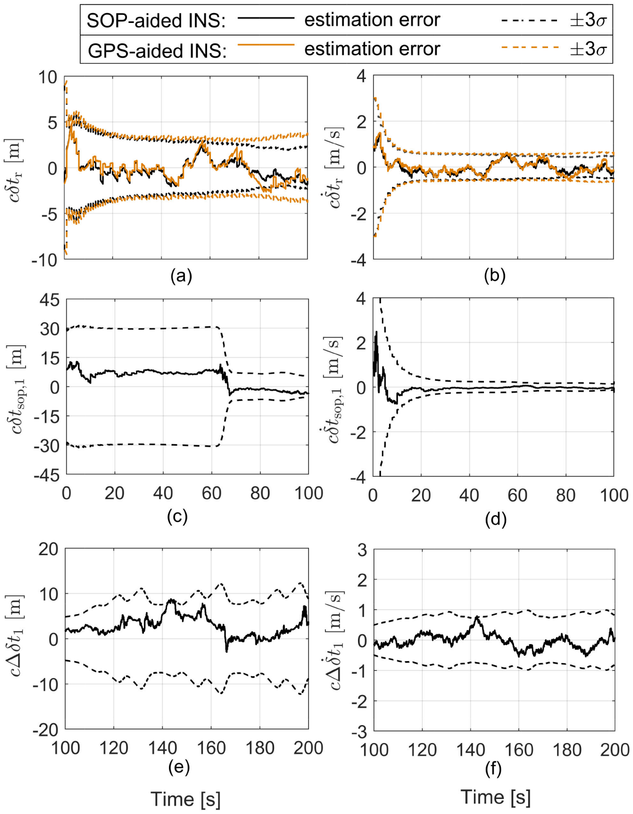

Fig. 8. Estimation error trajectories and ±3σ bounds for the clock states of the SOP-aided INS framework (black) and traditional GPS-aided INS (orange). (a) and (b) correspond to the receiver's clock bias $c\delta t_{\text{r}}$ and clock drift $c\dot{\delta t}_{\text{r}}$, respectively, while GPS was available and (c) and (d) correspond to SOP 1's clock bias $c\delta t_{\text{sop},1}$ and clock drift $c\dot{\delta t}_{\text{sop},1}$, respectively while GPS was available. (e) and (f) correspond to the relative bias $c\Delta\delta t_1$ and drift $c\Delta\dot{\delta t}_1$ between the UAV-mounted receiver and SOP 1 during the radio SLAM mode.

their equipped oscillators using the environment illustrated in Fig. 4.

1) *Varying Quantity of SOPs:* To study the performance sensitivity of the SOP-aided INS framework for a varying number of SOPs, six separate simulation runs were conducted. The first four runs employed the SOP-aided INS with a consumer-grade IMU and $M = 1, \ldots, 4$ SOPs. The last two runs employed a traditional tightly coupled GPS-INS and no SOPs ($M = 0$) with 1) a tactical-grade IMU and 2) a consumer-grade IMU. Fig. 9 illustrates the resulting logarithm of the determinant of the position estimation error covariance $\log\{\det[\mathbf{P}_{\boldsymbol{r}_b}(k|j)]\}$ for each run, which is related to the volume of the estimation uncertainty ellipsoid [30].

The following may be concluded from Fig. 9. First, the estimation uncertainties produced by the SOP-aided INS are reduced when M is increased, and the sensitivity of the estimation uncertainty to varying M is captured by the distance between the $\log\{\det[\mathbf{P}_{\boldsymbol{r}_b}]\}$ trajectories. Second, although the SOP-aided INS used a *consumer-grade* IMU, the position estimation uncertainty for $M = 1, \ldots, 4$ was always lower than the position estimation uncertainty produced by a traditional tightly coupled GPS-aided INS using a *tactical-grade* IMU. Third, the estimation uncertainties produced by the GPS-aided INS began to diverge unboundedly when GPS was cut off, whereas a bound may be specified for the uncertainties produced by the SOP-aided INS for $M = 1, \ldots, 4$.

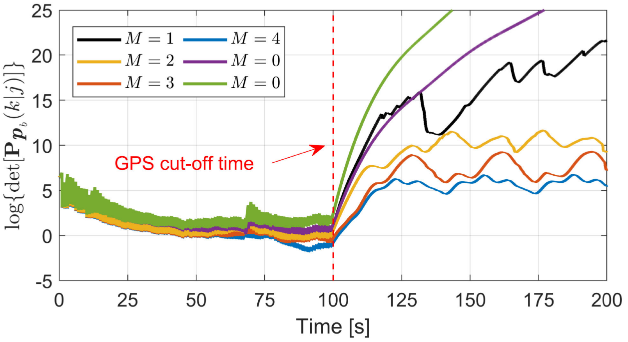

Fig. 9. Logarithm of the determinant of the estimation error covariance of the UAV's position states $\log\{\det[\mathbf{P}_{\boldsymbol{r}_b}(k|j)]\}$. The two curves for $M = 0$ correspond to a tightly-coupled GPS-aided INS equipped with a tactical-grade IMU (purple) and consumer-grade IMU (green). The curves for $M = 1, 2, 3, 4$ correspond to the tightly-coupled SOP-aided INS with a consumer-grade IMU for a varying number of SOPs. The GPS cutoff time is marked with a red dashed vertical line.

TABLE V
Quality of SOP Clocks

Quality	**parameters** $\{h_{0,\text{sop},m},\ h_{-2,\text{sop},m}\}$
Worst TCXO	$\{2.0 \times 10^{-19},\ 2.0 \times 10^{-20}\}$
Typical TCXO	$\{9.4 \times 10^{-20},\ 3.8 \times 10^{-21}\}$
Typical OCXO	$\{8.0 \times 10^{-20},\ 4.0 \times 10^{-23}\}$
Best OCXO	$\{2.6 \times 10^{-22},\ 4.0 \times 10^{-26}\}$

2) *Varying Quality of SOP Clocks:* To study the performance sensitivity of the SOP-aided INS framework for a varying quality of SOP clocks, four simulation runs were conducted, where in each run all four SOPs were assumed to be equipped with the same clock quality: 1) Worst TCXO, 2) typical TCXO, 3) typical OCXO, and 4) best OCXO. In all runs, the UAV-mounted receiver was assumed to be equipped with a typical TCXO. The characterizing parameters of the four oscillator grades are tabulated in Table V. The resulting 3σ bounds for exploiting four SOPs, which were assumed to all be equipped with a worst TCXO (black), typical TCXO (green), typical OCXO (blue), and best OCXO (purple), are plotted in Fig. 10. The four grades of oscillators considered and their characterizing parameters are tabulated in Table V.

From Fig. 10 it may be concluded that while GPS was available, the sensitivity of the estimation performance to SOP clock quality was minimal. When GPS pseudoranges become unavailable, the estimation performance was significantly more sensitive to the SOP clock quality, and the sensitivity is captured by the distance between the 3σ trajectories. Although the uncertainty in the estimates were larger when SOPs were equipped with a worst TCXO, a bound may still be established.

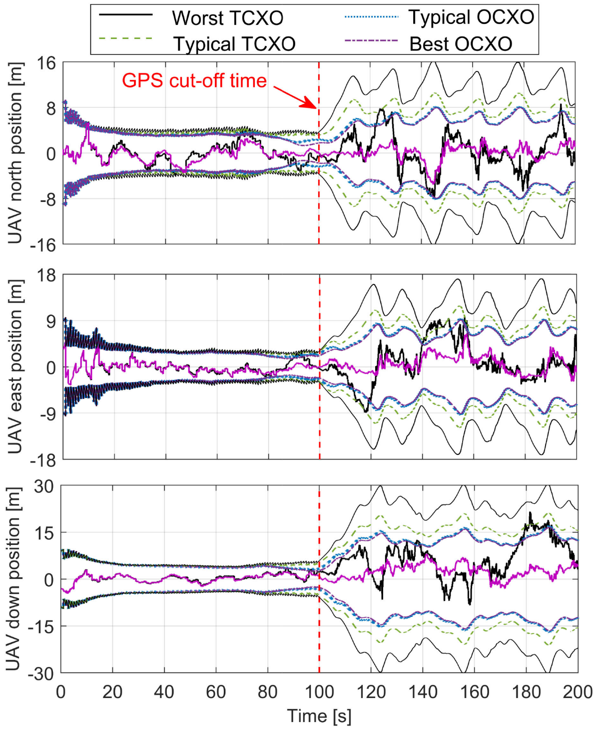

Fig. 10. Estimation error trajectories and $\pm 3\sigma$ bounds for the UAV's north, east, and down position states with the tightly coupled SOP-aided INS assuming all SOPs to be equipped with 1) worst TCXO (black), 2) Typical TCXO (green), 3) typical OCXO (blue), and 4) best OCXO (purple). The GPS cutoff time is marked with a red dashed vertical line.

VI. EXPERIMENTAL DEMONSTRATION

This section presents experimental results demonstrating a UAV navigating with the tightly coupled SOP-aided INS framework using real IMU data, signals from three cellular SOP transmitters, and signals from 11 GPS satellites (when available). For a comparative analysis, results are also presented of the UAV navigating with a traditional tightly coupled GPS-aided INS using the same IMU data and GPS signals. The following experiment was conducted by collecting the IMU, GPS, and SOP data in the field, after which the data were postprocessed in the lab. The experiment used an Autel Robotics UAV [60] equipped with the following.

1) Tri-band (144/400/1200 MHz) cellular omnidirectional antenna from Ettus Research [61].
2) Consumer-grade L1 GPS active patch antenna from QGP Supply [62].
3) Dual-channel USRP from Ettus Research [63], which was used to simultaneously downmix and sample cellular CDMA signals at 3.2 mega-samples per second (MSPS). Pseudoranges to three cellular SOPs were extracted from these samples at 5 Hz by processing them through the Multichannel Adaptive TRansceiver Information eXtractor (MATRIX) software-defined radio (SDR) [13], [57], developed by the Autonomous Systems Perception, Intelligence, and Navigation (ASPIN) Laboratory at the University of California, Irvine.
4) Proprietary consumer-grade IMU, developed by Autel Robotics. The Autel Robotics UAV allows access to raw IMU data, which were used for the time update at 100 Hz of the orientation, position, and velocity of the UAV as illustrated in Fig. 3. The IMU data are also coupled with altimeter and GPS data in the UAV's onboard navigation system to produce an integrated navigation solution. The UAV allows access to this navigation solution, which was used as the ground truth result with which the proposed tightly-coupled SOP-aided INS framework was compared.

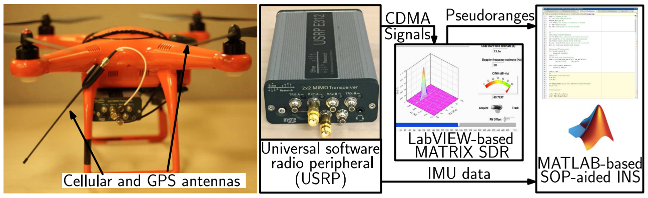

Fig. 11. Experiment software and hardware setup.

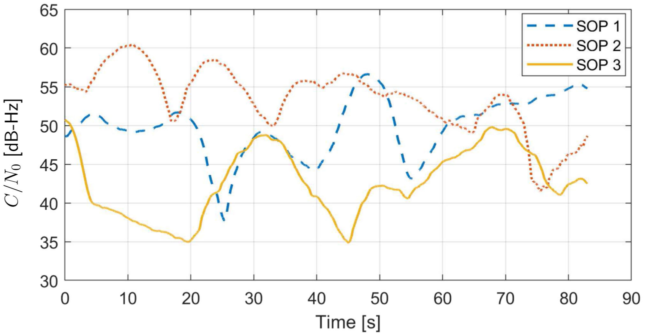

Fig. 12. Time history of C/N_0 for SOP 1,2, and 3, produced by the MATRIX SDR.

Fig. 11 depicts the experimental software and hardware setup.

The following experiment was conducted by collecting the IMU, GPS, and SOP data and then postprocessing the data in the lab. The UAV was commanded to traverse the trajectory plotted in Fig. 13(a), in which GPS was available for the first 50 s, then unavailable for the last 30 s. The SOP-aided INS framework was initialized with a state estimate given by

$$\hat{\boldsymbol{x}}(0|0) = \left[\hat{\boldsymbol{x}}^{\mathsf{T}}_{\text{gnss,ins}}(0|0), \hat{\boldsymbol{x}}^{\mathsf{T}}_{\text{sop},1}(0|0), \ldots, \hat{\boldsymbol{x}}^{\mathsf{T}}_{\text{sop},3}(0|0)\right]^{\mathsf{T}}$$

where the estimates of orientation ${}^{b}_{e}\hat{\bar{\boldsymbol{q}}}(0|0)$, position ${}^{e}\hat{\boldsymbol{r}}_b(0|0)$, and velocity ${}^{e}\hat{\dot{\boldsymbol{r}}}_b(0|0)$ were set to values parsed from the beginning of the UAV's navigation system log files, which were recorded during the trajectory, and the IMU biases $\hat{\boldsymbol{b}}_{\text{gyr}}$ and $\hat{\boldsymbol{b}}_{\text{acc}}$ were initialized by averaging 5 s of gravity-compensated IMU measurements while the vehicle was stationary and after the IMU had warmed up. The cellular

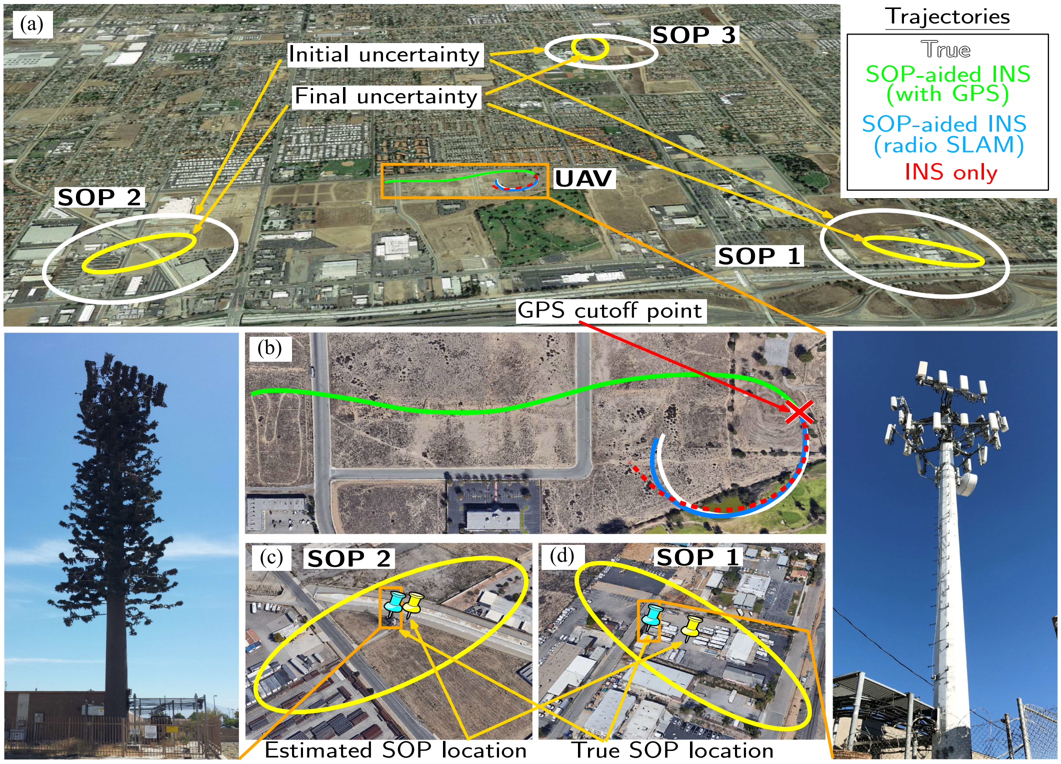

Fig. 13. (a) Experimental environment showing the UAV's trajectory, cellular SOPs' locations, initial SOPs' position uncertainties, and final position uncertainties. (b) UAV's trajectory before and after GPS cutoff: 1) White: Ground truth, 2) Green: SOP-aided INS before GPS cutoff, 3) Blue: SOP-aided INS after GPS cutoff, and 4) Red: GPS aided INS after GPS cutoff, i.e., INS only. (c) and (d) True and estimated SOP locations and corresponding final uncertainty ellipses. A vector graphics editor was used to trace the trajectories and ellipses for easier viewing.

SOP transmitters' initial state estimates were drawn according to $\hat{\boldsymbol{x}}_{\text{sop},m}(0|0) \sim \mathcal{N}([{}^{e}\boldsymbol{r}^{\mathsf{T}}_{\text{sop},m}, \boldsymbol{x}^{\mathsf{T}}_{\text{clk,sop},m}(0)]^{\mathsf{T}}, \mathbf{P}_{\text{sop},m}(0|0))$. The true transmitters' positions $\{{}^{e}\boldsymbol{r}_{\text{sop},m}\}_{m=1}^{3}$ were surveyed beforehand according to the framework described in [64] and verified using Google Earth. The initial clock bias and drift

$$\boldsymbol{x}_{\text{clk,sop},m}(0) = c\left[\delta t_{\text{sop},m}(0),\ \dot{\delta t}_{\text{sop},m}(0)\right]^{\mathsf{T}} \quad m = 1, \ldots, 3$$

were solved for by using the initial set of cellular transmitter pseudoranges (11) according to

$$c\delta t_{\text{sop},m}(0) = \|{}^{e}\boldsymbol{r}_b(0) - {}^{e}\boldsymbol{r}_{\text{sop},m}\| + c\delta t_r(0) - z_{\text{sop},m}(0)$$
$$c\dot{\delta t}_{\text{sop},m}(0) = [\delta t_{\text{sop},m}(1) - \delta t_{\text{sop},m}(0)]/T$$

where $c\delta t_{\text{sop},m}(1) = \|{}^{e}\boldsymbol{r}_b(1) - {}^{e}\boldsymbol{r}_{\text{sop},m}\| + c\delta t_r(1) - z_{\text{sop},m}(1)$ and the receiver's clock bias $c\delta t_r(0)$ was provided by the GPS receiver while GPS was available.

The corresponding estimation error covariance was initialized according to

$$\mathbf{P}(0|0) = \text{diag}\left[\mathbf{P}_{\text{gnss,ins}}(0|0), \mathbf{P}_{\text{sop},1}(0|0), \ldots, \mathbf{P}_{\text{sop},3}(0|0)\right]$$
$$\mathbf{P}_{\boldsymbol{x}_{\text{gnss,ins}}}(0|0) \triangleq \text{diag}\left[\mathbf{P}_{\boldsymbol{x}_{\text{imu}}}(0|0),\ \mathbf{P}_{\boldsymbol{x}_{\text{clk,r}}}(0|0)\right]$$
$$\mathbf{P}_{\boldsymbol{x}_{\text{imu}}}(0|0) \equiv \text{diag}\left[(10^{-1})\cdot\mathbf{I}_{3\times3},\ 9\cdot\mathbf{I}_{3\times3},\ \mathbf{I}_{3\times3},\ (10^{-4})\cdot\mathbf{I}_{6\times6}\right]$$
$$\mathbf{P}_{\boldsymbol{x}_{\text{clk,r}}}(0|0) \equiv \text{diag}\left[0.1,\ 0.01\right]$$
$$\mathbf{P}_{\text{sop},m}(0|0) \equiv 10^{4}\cdot\text{diag}\left[\mathbf{I}_{3\times3}, 0.3, 0.03\right], \quad m = 1, 2, 3.$$

Signals may be acquired later in the run from SOPs that were not initialized in the EKF while the receiver had access to GPS. Although this case is not considered in this experiment, it is worth mentioning here that a batch filter that uses pseudoranges collected over a short window of time may be used to initialize the estimates of the newly acquired SOP's in the absence of GPS [65]. To incorporate the uncertainty of the vehicle's position states, these states may be added to the estimated vector and the INS-produced vehicle's position may be fed as measurements along with the SOP pseudoranges.

The process noise covariance of the receiver's clock $\mathbf{Q}_{\text{clk,r}}$ was set to correspond to a typical TCXO. The process noise covariances of the cellular transmitters' clocks were set to correspond to a typical OCXO, which is usually the case for cellular transmitters [66], [67]. The power spectral density matrices associated with the gyroscope and accelerometer noise were set to $\mathbf{S}_{\boldsymbol{n}_{\text{gyr}}} \equiv (7\times10^{-4})^2\cdot\mathbf{I}_{3\times3}$ and $\mathbf{S}_{\boldsymbol{n}_{\text{acc}}} \equiv (5\times10^{-4})^2\cdot\mathbf{I}_{3\times3}$, respectively. The power spectral density matrices associated with the gyroscope and accelerometer bias variations were set to $\mathbf{S}_{\boldsymbol{w}_{\text{gyr}}} \equiv (1\times10^{-4})^2\cdot\mathbf{I}_{3\times3}$ $\mathbf{S}_{\boldsymbol{w}_{\text{acc}}} \equiv (1\times10^{-4})^2\cdot\mathbf{I}_{3\times3}$, whose values were found empirically using raw IMU data. These spectra are mapped to the discrete-time noise covariances $\mathbf{Q}_{\boldsymbol{n}_{\text{gyr}}}$, $\mathbf{Q}_{\boldsymbol{n}_{\text{acc}}}$, $\mathbf{Q}_{\boldsymbol{w}_{\text{gyr}}}$, and $\mathbf{Q}_{\boldsymbol{w}_{\text{acc}}}$ online through the equations provided in Appendix B. The measurement noise variances $\{\sigma^2_{\text{sop},m}\}_{m=1}^{3}$ were computed according to (20), except that $\sigma^2_{\text{gnss},n,j}$ is replaced with $\sigma^2_{\text{sop},m,j}$, $T_c \equiv 1/(1.2288\times10^{6})$, $\sigma_s \equiv 10$, $T_{CO} \equiv 1/37.5$ s, and the carrier-to-noise ratio C/N_0 produced by the MATRIX SDR for each SOP was used. Note that the C/N_0

TABLE VI
Experimental Estimation Errors After GPS Cutoff

Estimation framework	**RMSE [m]**	**Final error [m]**
INS only	18.94	57.30
SOP-aided INS	5.84	9.59

produced by an SOP SDR could be used in real time to create a time-varying measurement noise variance for the EKF. The time history of C/N_0 for each SOP is illustrated in Fig. 12.

The UAV flew in the vicinity of three cellular SOPs with an initial uncertainty ellipsoid illustrated in Fig. 13(a). It can be seen in Fig. 13(b) that after the GPS cutoff point, the INS only solution (red) began to drift from the truth, resulting in a large final error. On the other hand, the tightly coupled SOP-aided INS solution (green) prevented this drift by using the pseudoranges drawn from the three cellular SOPs, resulting in a significantly reduced final error. The north-east root mean squared error (RMSE) and final error for 1) GPS-aided INS framework after GPS cutoff (i.e., INS only) and 2) SOP-aided INS framework after GPS cutoff are summarized in Table. VI. The final estimated transmitter location and corresponding 95th–percentile uncertainty ellipse for two of the SOP transmitters are shown in Fig. 13(c)–(d). The final localization errors for the three SOPs were 26.6, 19.6, and 59.1 m, respectively.

Note the following two points from these results. First, the final error of the UAV's position is smaller than the SOPs' position errors. Since the SOP-aided INS is EKF-based and the UAV has *a priori* knowledge of its state, the UAV's final position error can be smaller than the aiding sources' final position errors. The UAV's position error and uncertainty may grow in this time window and the growth rate is dependent on IMU quality, the uncertainty in the SOPs' positions and clock states, and measurement quality. However, the pseudorange measurements from the SOPs are still significantly decreasing the error and uncertainty growth rate compared to an INS alone. Second, the relatively large estimation error of the third SOP is mostly attributed to a lower carrier-to-noise ratio compared to the other SOPs, which results in a higher measurement noise variance. Also, there was a small number of outliers in the pseudorange measurements that were not removed. To further enhance performance, these outliers may be detected and the SOP responsible for the outliers may be temporarily excluded using a RAIM approach for SOPs [58]. Despite not removing the small number of outlier pseudorange measurements, the final position error was smaller than the initial uncertainty and the position estimate was captured within the final estimation uncertainty ellipse.

VII. CONCLUSION

This article developed and studied an SOP-aided INS framework. The performance of the framework was compared against a traditional tightly coupled GNSS-aided INS integration strategy and the performance sensitivity was studied by varying the quantity and quality of exploited SOPs. The SOP-aided INS was shown to possess several advantages over the GNSS-aided INS. When GNSS signals are available, incorporating ambient terrestrial SOPs produces a more accurate navigation solution compared to using GNSS alone. A bound appears to be established on the estimation errors in the absence of GNSS. The SOP-aided INS may relax requirements on IMU quality. For example, using a consumer-grade IMU was shown to produce estimation uncertainties lower than a traditional tightly coupled GNSS-aided INS using a tactical-grade IMU when two, three, or four SOPs were exploited. Furthermore, it was shown that SOPs equipped with low-quality oscillators may serve as effective INS-aiding sources to establish a bound on INS errors in the absence of GNSS for a finite-time horizon. Moreover, experimental results demonstrated a vehicle navigating with the SOP-aided INS framework in the absence of GNSS, which yielded an RMSE reduction of 59.9% when compared to an unaided INS.

APPENDIX

A. TIME UPDATE OF $\boldsymbol{x}_{\text{imu}}$

The time update of $\boldsymbol{x}_{\text{imu}}$ is performed using ECEF strapdown mechanization equations.

1 Orientation Time Update

The orientation time update is given by

$$ {}^{b}_{e}\hat{\bar{\boldsymbol{q}}}(k+1|j) = {}^{b_{k+1}}_{b_k}\hat{\bar{\boldsymbol{q}}} \otimes {}^{b}_{e}\hat{\bar{\boldsymbol{q}}}(k|j) \tag{21} $$

where ${}^{b_{k+1}}_{b_k}\hat{\bar{\boldsymbol{q}}}$ represents an estimate of the rotation quaternion between the IMU's body frame at time k and $k+1$. The quaternion ${}^{b_{k+1}}_{b_k}\hat{\bar{\boldsymbol{q}}}$ is computed by integrating gyroscope rotation rate data $\boldsymbol{\omega}_{\text{imu}}(k)$ and $\boldsymbol{\omega}_{\text{imu}}(k+1)$ using a fourth order Runge-Kutta according to

$$ {}^{b_{k+1}}_{b_k}\hat{\bar{\boldsymbol{q}}} = \bar{\boldsymbol{q}}_0 + \frac{T}{6}\left(\boldsymbol{d}_1 + 2\boldsymbol{d}_2 + 2\boldsymbol{d}_3 + \boldsymbol{d}_4\right) $$

where

$$ \boldsymbol{d}_1 = \frac{1}{2}\boldsymbol{\Omega}\left[{}^{b}\hat{\boldsymbol{\omega}}(k)\right]\bar{\boldsymbol{q}}_0, \quad \boldsymbol{d}_2 = \frac{1}{2}\boldsymbol{\Omega}\left[\bar{\boldsymbol{\omega}}\right]\cdot\left(\bar{\boldsymbol{q}}_0 + \frac{1}{2}T\boldsymbol{d}_1\right) $$

$$ \boldsymbol{d}_3 = \frac{1}{2}\boldsymbol{\Omega}\left[\bar{\boldsymbol{\omega}}\right]\cdot\left(\bar{\boldsymbol{q}}_0 + \frac{1}{2}T\boldsymbol{d}_2\right) $$

$$ \boldsymbol{d}_4 = \frac{1}{2}\boldsymbol{\Omega}\left[{}^{b}\hat{\boldsymbol{\omega}}(k+1)\right]\cdot\left(\bar{\boldsymbol{q}}_0 + T\boldsymbol{d}_3\right), \quad \bar{\boldsymbol{q}}_0 \triangleq [0,\ 0,\ 0,\ 1]^{\mathsf{T}} $$

$$ \bar{\boldsymbol{\omega}} \triangleq \frac{1}{2}\left[{}^{b}\hat{\boldsymbol{\omega}}(k) + {}^{b}\hat{\boldsymbol{\omega}}(k+1)\right] - {}^{e}_{b}\mathbf{R}^{\mathsf{T}}(k)\,{}^{e}_{i}\boldsymbol{\omega} $$

where $\boldsymbol{\Omega}[\,\cdot\,] \in \mathbb{R}^{4\times4}$ is given by

$$ \boldsymbol{\Omega}\left[\boldsymbol{a}\right] \triangleq \begin{bmatrix} -\lfloor \boldsymbol{a}\times\rfloor & \boldsymbol{a} \\ -\boldsymbol{a}^{\mathsf{T}} & 0 \end{bmatrix}, \quad \boldsymbol{a} \triangleq [a_1, a_2, a_3]^{\mathsf{T}} $$

${}^{b}\hat{\boldsymbol{\omega}}(k)$ is the bias-compensated rotation rate measurement, which is computed according to

$$ {}^{b}\hat{\boldsymbol{\omega}}(k) = \boldsymbol{\omega}_{\text{imu}}(k) - \hat{\boldsymbol{b}}_{\text{gyr}}(k|j) \tag{22} $$

and ${}^{e}_{i}\boldsymbol{\omega} \triangleq [0,\ 0,\ {}^{e}_{i}\omega]^{\mathsf{T}}$ is the rotation rate of the Earth, i.e., the rotation rate of the ECEF frame $\{e\}$ with respect to the ECI frame $\{i\}$. The value of ${}^{e}_{i}\omega$, according to the latest version of the world geodetic system (WGS 84), is ${}^{e}_{i}\omega = 7.292\,115 \times 10^{-5}$ rad/s.

2 Position and Velocity Time Update

Integrating IMU specific force data to perform a time update of the position and velocity in an ECEF coordinate frame introduces a centrifugal and Coriolis term due to the rotation rate of the Earth ${}^{e}_{i}\boldsymbol{\omega}$ [48]. Assuming that the variation of the Coriolis force is negligible over the integration interval, the velocity time update is performed according to

$$ \begin{aligned} {}^{e}\hat{\dot{\boldsymbol{r}}}_{b}(k+1|j) = {}^{e}\hat{\dot{\boldsymbol{r}}}_{b}(k|j) + \frac{T}{2}\left[{}^{e}\hat{\boldsymbol{a}}(k) + {}^{e}\hat{\boldsymbol{a}}(k+1)\right] \\ + {}^{e}\boldsymbol{g}(k, {}^{e}\boldsymbol{r}_{b}(k))T - 2T\lfloor {}^{i}_{e}\boldsymbol{\omega}\times\rfloor {}^{e}\hat{\dot{\boldsymbol{r}}}_{b}(k|j) \end{aligned} \tag{23} $$

where ${}^{e}\hat{\boldsymbol{a}}$ and ${}^{b}\boldsymbol{a}$ are the transformed bias-compensated specific force and untransformed bias-compensated specific force, respectively, which are given by

$$ {}^{e}\hat{\boldsymbol{a}}(k) \triangleq \hat{\mathbf{R}}^{\mathsf{T}}(k)\,{}^{b}\hat{\boldsymbol{a}}(k) \tag{24} $$

$$ {}^{b}\boldsymbol{a}(k) = \hat{\boldsymbol{a}}_{\text{imu}}(k) - \hat{\boldsymbol{b}}_{\text{acc}}(k|j) \tag{25} $$

and $\hat{\mathbf{R}}(k) \triangleq \mathbf{R}[{}^{b}_{e}\hat{\bar{\boldsymbol{q}}}(k|j)]$.

The position time update is performed according to

$$ \begin{aligned} {}^{e}\hat{\boldsymbol{r}}_{b}(k+1|j) = {}^{e}\hat{\boldsymbol{r}}_{b}(k|j) + \frac{T}{2}\left[{}^{e}\hat{\dot{\boldsymbol{r}}}_{b}(k+1|j) + {}^{b}\hat{\dot{\boldsymbol{r}}}(k|j)\right] \\ - T^{2}\lfloor {}^{i}_{e}\boldsymbol{\omega}\times\rfloor {}^{e}\hat{\dot{\boldsymbol{r}}}_{b}(k|j). \end{aligned} \tag{26} $$

3 Accelerometer and Gyroscope Bias Time Update

The time update of the biases $\boldsymbol{b}_{\text{gyr}}$ and $\boldsymbol{b}_{\text{acc}}$ follow from (1) and (2), respectively, giving

$$ \hat{\boldsymbol{b}}_{\text{gyr}}(k+1|j) = \hat{\boldsymbol{b}}_{\text{gyr}}(k|j) $$

$$ \hat{\boldsymbol{b}}_{\text{acc}}(k+1|j) = \hat{\boldsymbol{b}}_{\text{acc}}(k|j). $$

B. INS STATE TRANSITION AND PROCESS NOISE COVARIANCE MATRICES

The calculation of the discrete-time linearized INS state transition matrix $\boldsymbol{\Phi}_{\text{imu}}$ and process noise covariance $\mathbf{Q}_{\text{imu}}$ are performed using strapdown INS equations as described in [48] and [68]. The discrete-time linearized INS state transition matrix $\boldsymbol{\Phi}_{\text{imu}}$ is given by

$$ \boldsymbol{\Phi}_{\text{imu}} = \begin{bmatrix} \boldsymbol{\Phi}_{\boldsymbol{qq}} & \mathbf{0}_{3\times3} & \mathbf{0}_{3\times3} & \boldsymbol{\Phi}_{\boldsymbol{qb}_{\text{gyr}}} & \mathbf{0}_{3\times3} \\ \boldsymbol{\Phi}_{\boldsymbol{rq}} & \mathbf{I}_{3\times3} & T\mathbf{I}_{3\times3} & \boldsymbol{\Phi}_{\boldsymbol{rb}_{\text{gyr}}} & \boldsymbol{\Phi}_{\boldsymbol{rb}_{\text{acc}}} \\ \boldsymbol{\Phi}_{\dot{\boldsymbol{r}}\boldsymbol{q}} & \mathbf{0}_{3\times3} & \boldsymbol{\Phi}_{\dot{\boldsymbol{r}}\dot{\boldsymbol{r}}} & \boldsymbol{\Phi}_{\dot{\boldsymbol{r}}\boldsymbol{b}_{\text{gyr}}} & \boldsymbol{\Phi}_{\dot{\boldsymbol{r}}\boldsymbol{b}_{\text{acc}}} \\ \mathbf{0}_{3\times3} & \mathbf{0}_{3\times3} & \mathbf{0}_{3\times3} & \mathbf{I}_{3\times3} & \mathbf{0}_{3\times3} \\ \mathbf{0}_{3\times3} & \mathbf{0}_{3\times3} & \mathbf{0}_{3\times3} & \mathbf{0}_{3\times3} & \mathbf{I}_{3\times3} \end{bmatrix} $$

where

$$ \boldsymbol{\Phi}_{\boldsymbol{qq}} = \mathbf{I}_{3\times3} - T\lfloor {}^{e}_{i}\boldsymbol{\omega}\times\rfloor, \quad \boldsymbol{\Phi}_{\dot{\boldsymbol{r}}\dot{\boldsymbol{r}}} = \mathbf{I}_{3\times3} - 2T\lfloor {}^{e}_{i}\boldsymbol{\omega}\times\rfloor $$

$$ \boldsymbol{\Phi}_{\boldsymbol{qb}_{\text{gyr}}} = -\frac{T}{2}\left[\hat{\mathbf{R}}^{\mathsf{T}}(k+1) + \hat{\mathbf{R}}^{\mathsf{T}}(k)\right] $$

$$ \boldsymbol{\Phi}_{\dot{\boldsymbol{r}}\boldsymbol{q}} = -\frac{T}{2}\left\lfloor\left[{}^{e}\hat{\boldsymbol{a}}(k) + {}^{e}\hat{\boldsymbol{a}}(k+1)\right]\times\right\rfloor, \quad \boldsymbol{\Phi}_{\boldsymbol{rq}} = \frac{T}{2}\boldsymbol{\Phi}_{\dot{\boldsymbol{r}}\boldsymbol{q}} $$

$$ \boldsymbol{\Phi}_{\dot{\boldsymbol{r}}\boldsymbol{b}_{\text{gyr}}} = -\frac{T}{2}\lfloor {}^{e}\hat{\boldsymbol{a}}(k)\times\rfloor\boldsymbol{\Phi}_{\boldsymbol{qb}_{\text{gyr}}}, \quad \boldsymbol{\Phi}_{\dot{\boldsymbol{r}}\boldsymbol{b}_{\text{acc}}} = \boldsymbol{\Phi}_{\boldsymbol{qb}_{\text{gyr}}} $$

$$ \boldsymbol{\Phi}_{\boldsymbol{rb}_{\text{gyr}}} = \frac{T}{2}\boldsymbol{\Phi}_{\dot{\boldsymbol{r}}\boldsymbol{b}_{\text{gyr}}}, \quad \boldsymbol{\Phi}_{\boldsymbol{rb}_{\text{acc}}} = \frac{T}{2}\boldsymbol{\Phi}_{\dot{\boldsymbol{r}}\boldsymbol{b}_{\text{acc}}}. $$

The discrete-time linearized INS process noise covariance $\mathbf{Q}_{\text{imu}}$ is given by

$$ \mathbf{Q}_{\text{imu}} = \frac{T}{2}\boldsymbol{\Phi}_{\text{imu}}\mathbf{N}_{c}\boldsymbol{\Phi}_{\text{imu}}^{\mathsf{T}} + \mathbf{N}_{c} $$

where

$$ \mathbf{N}_{c} = \text{diag}\left[\mathbf{S}_{\boldsymbol{n}_{\text{gyr}}},\ \mathbf{0}_{3\times3},\ \mathbf{S}_{\boldsymbol{n}_{\text{acc}}},\ \mathbf{S}_{\boldsymbol{w}_{\text{gyr}}},\ \mathbf{S}_{\boldsymbol{w}_{\text{acc}}}\right] $$

where $\mathbf{S}_{\boldsymbol{n}_{\text{gyr}}} = T\mathbf{Q}_{\boldsymbol{n}_{\text{gyr}}}$ and $\mathbf{S}_{\boldsymbol{n}_{\text{acc}}} = T\mathbf{Q}_{\boldsymbol{n}_{\text{acc}}}$ are the PSD matrices of the gyroscope's and accelerometer's random noise, respectively, and $\mathbf{S}_{\boldsymbol{w}_{\text{gyr}}} = \mathbf{Q}_{\boldsymbol{w}_{\text{gyr}}}/T$ and $\mathbf{S}_{\boldsymbol{w}_{\text{acc}}} = \mathbf{Q}_{\boldsymbol{w}_{\text{acc}}}/T$ are the PSD matrices of the gyroscope's and accelerometer's bias variation, respectively.

C. EKF STATE MEASUREMENT UPDATE EQUATIONS

The standard EKF equations are modified to deal with the 3D orientation error correction, which contains one less dimension than the 4D orientation quaternion estimate, as described in Section IV-B. To this end, the state estimate is separated into two parts according to $\hat{\boldsymbol{x}} \triangleq [{}^{b}_{e}\hat{\bar{\boldsymbol{q}}}^{\mathsf{T}}, \hat{\boldsymbol{y}}^{\mathsf{T}}]^{\mathsf{T}}$, where ${}^{b}_{e}\hat{\bar{\boldsymbol{q}}} \in \mathbb{R}^{4}$ is the orientation quaternion estimate and $\hat{\boldsymbol{y}} \in \mathbb{R}^{14+5\,M}$ is a vector containing the remaining estimates of $\boldsymbol{x}$. Next, the EKF correction vector $\breve{\boldsymbol{x}}(k+1)$, which is to be applied to the current state prediction $\hat{\boldsymbol{x}}(k+1|j)$ to produce the EKF state measurement update $\hat{\boldsymbol{x}}(k+1|k+1)$, is computed according to

$$ \breve{x}(k+1) \triangleq \begin{bmatrix} \breve{\boldsymbol{\theta}}(k+1) \\ \breve{\boldsymbol{y}}(k+1) \end{bmatrix} = \begin{bmatrix} \boldsymbol{\Lambda}_{\boldsymbol{\theta}}\mathbf{K}(k+1)\boldsymbol{\nu}(k+1|j) \\ \boldsymbol{\Lambda}_{\boldsymbol{y}}\mathbf{K}(k+1)\boldsymbol{\nu}(k+1|j) \end{bmatrix} $$

where $\breve{\boldsymbol{\theta}} \in \mathbb{R}^{3}$ is the orientation correction, $\breve{\boldsymbol{y}} \in \mathbb{R}^{14+5\,M}$ is a vector containing the remaining corrections

$$ \boldsymbol{\Lambda}_{\boldsymbol{\theta}} \triangleq \left[\mathbf{I}_{3\times3}, \mathbf{0}_{3\times(14+5\,M)}\right] $$

$$ \boldsymbol{\Lambda}_{\boldsymbol{y}} \triangleq \left[\mathbf{0}_{(14+5\,M)\times3}, \mathbf{I}_{(14+5\,M)\times(14+5\,M)}\right] $$

$\boldsymbol{\nu}(k+1|j) \triangleq \boldsymbol{z}(k+1) - \hat{\boldsymbol{z}}(k+1|j)$ is the measurement residual, and $\mathbf{K}$ and $\mathbf{S}$ are defined in (18) and (19), respectively. Finally, the EKF state measurement update $\boldsymbol{x}(k+1|k+1)$ is computed by applying $\breve{\boldsymbol{\theta}}(k+1)$ to ${}^{b}_{e}\hat{\bar{\boldsymbol{q}}}(k+1|j)$

through (14), and applying $\breve{\boldsymbol{y}}(k+1)$ to $\boldsymbol{y}(k+1|j)$ using the standard EKF additive update equation, giving

$$\hat{\boldsymbol{x}}(k+1|k+1) =$$
$$\begin{bmatrix} {}^{b}_{e}\hat{\bar{\boldsymbol{q}}}(k+1|j) \otimes \begin{bmatrix} \frac{1}{2}\breve{\boldsymbol{\theta}}^{\mathsf{T}}(k+1), \sqrt{1-\frac{1}{4}\breve{\boldsymbol{\theta}}^{\mathsf{T}}(k+1)\breve{\boldsymbol{\theta}}(k+1)} \end{bmatrix}^{\mathsf{T}} \\ \hat{\boldsymbol{y}}(k+1|j)+\breve{\boldsymbol{y}}(k+1) \end{bmatrix}.$$

ACKNOWLEDGMENT

The authors would like to thank J. Khalife for his help with data collection, P. Roysdon for his help with data simulation, and Prof. M. Braasch for helpful discussions that improved the quality of this article.

REFERENCES

[1] S. Ji, W. Chen, X. Ding, Y. Chen, C. Zhao, and C. Hu
Potential benefits of GPS/GLONASS/GALILEO integration in an urban canyon - Hong Kong
J. Navigation, vol. 63, no. 4, pp. 681–693, Oct. 2010.

[2] R. Ioannides, T. Pany, and G. Gibbons
Known vulnerabilities of global navigation satellite systems, status, and potential mitigation techniques
Proc. IEEE, vol. 104, no. 6, pp. 1174–1194, Jun. 2016.

[3] M. Li and A. Mourikis
High-precision, consistent EKF-based visual-inertial odometry
Int. J. Robot. Res., vol. 32, no. 6, pp. 690–711, May 2013.

[4] A. Soloviev
Tight coupling of GPS, INS, and laser for urban navigation
IEEE Trans. Aerosp. Electron. Syst., vol. 46, no. 4, pp. 1731–1746, Oct. 2010.

[5] G. Grenon, P. An, S. Smith, and A. Healey
Enhancement of the inertial navigation system for the morpheus autonomous underwater vehicles
IEEE J. Ocean. Eng., vol. 26, no. 4, pp. 548–560, Oct. 2001.

[6] Y. Wu, C. Goodall, and N. El-Sheimy
Self-calibration for IMU/odometer land navigation: Simulation and test results
In *Proc. ION Int. Tech. Meeting*, 2010, pp. 839–849.

[7] J. Petit, B. Stottelaar, M. Feiri, and F. Kargl
Remote attacks on automated vehicles sensors: Experiments on camera and Lidar
Black Hat Europe, vol. 11, 2015.

[8] Z. Kassas
Collaborative opportunistic navigation
IEEE Aerosp. Electron. Syst. Mag., vol. 28, no. 6, pp. 38–41, Jun. 2013.

[9] J. McEllroy
Navigation using signals of opportunity in the AM transmission band
Master's thesis, Air Force Institute of Technology, Wright-Patterson Air Force Base, Ohio, USA, 2006.

[10] S. Fang, J. Chen, H. Huang, and T. Lin
Is FM a RF-based positioning solution in a metropolitan-scale environment? A probabilistic approach with radio measurements analysis
IEEE Trans. Broadcast., vol. 55, no. 3, pp. 577–588, Sep. 2009.

[11] A. Popleteev
Indoor positioning using FM radio signals
Ph.D. dissertation, University of Trento, Trento, Italy, 2011.

[12] C. Yang and T. Nguyen
Tracking and relative positioning with mixed signals of opportunity
NAVIGATION,J. Inst. Navigation, vol. 62, no. 4, pp. 291–311, Dec. 2015.

[13] Z. Kassas, J. Khalife, K. Shamaei, and J. Morales
I hear, therefore I know where I am: Compensating for GNSS limitations with cellular signals
IEEE Signal Process. Mag.
pp. 111–124, Sep. 2017.

[14] J. Khalife and Z. Kassas
Navigation with cellular CDMA signals - Part II: Performance analysis and experimental results
IEEE Trans. Signal Process., vol. 66, no. 8, pp. 2204–2218, Apr. 2018.

[15] J. del Peral-Rosado, J. Lpez-Salcedo, F. Zanier, and G. Seco-Granados
Position accuracy of joint time-delay and channel estimators in LTE networks
IEEE Access, vol. 6, pp. 25185–25199, 2018.

[16] K. Shamaei and Z. Kassas
LTE receiver design and multipath analysis for navigation in urban environments
NAVIGATION, *J. Inst. Navigation*, vol. 65, no. 4, pp. 655–675, Dec. 2018.

[17] M. Rabinowitz and J. Spilker, Jr.
A new positioning system using television synchronization signals
IEEE Trans. Broadcast., vol. 51, no. 1, pp. 51–61, Mar. 2005.

[18] P. Thevenon *et al.*
Positioning using mobile TV based on the DVB-SH standard
NAVIGATION, *J. Inst. Navigation*, vol. 58, no. 2, pp. 71–90, 2011.

[19] J. Yang, X. Wang, M. Rahman, S. Park, H. Kim, and Y. Wu
A new positioning system using DVB-T2 transmitter signature waveforms in single frequency networks
IEEE Trans. Broadcast., vol. 58, no. 3, pp. 347–359, Sep. 2012.

[20] D. Lawrence *et al.*
Navigation from LEO: Current capability and future promise
GPS World Mag., vol. 28, no. 7, pp. 42–48, Jul. 2017.

[21] T. Reid, A. Neish, T. Walter, and P. Enge
Broadband LEO constellations for navigation
NAVIGATION, J. Inst. Navigation, vol. 65, no. 2, pp. 205–220, 2018.

[22] C. Ardito, J. Morales, J. Khalife, A. Abdallah, and Z. Kassas
Performance evaluation of navigation using LEO satellite signals with periodically transmitted satellite positions
In *Proc. ION Int. Tech. Meeting Conf.*, 2019, pp. 306–318.

[23] Z. Kassas, J. Morales, and J. Khalife
New-age satellite-based navigation - STAN: Simultaneous tracking and navigation with LEO satellite signals
Inside GNSS Mag., vol. 14, no. 4, pp. 56–65, 2019.

[24] Z. Kassas, J. Khalife, M. Neinavaie, and T. Mortlock
Opportunity comes knocking: Overcoming GPS vulnerabilities with other satellites' signals Inside Unmanned Systems Magazine. New York, NY, USA
Jun./Jul. 2020, pp. 30–35.

[25] J. Khalife, M. Neinavaie, and Z. Kassas
Navigation with differential carrier phase measurements from megaconstellation LEO satellites
In *Proc. IEEE/ION Position, Location, Navigation Symp.*, Apr. 2020, pp. 1393–1404.

[26] R. Faragher and R. Harle
Towards an efficient, intelligent, opportunistic smartphone indoor positioning system
NAVIGATION,J. Inst. Navigation, vol. 62, no. 1, pp. 55–72, 2015.

[27] Y. Zhuang, Z. Syed, Y. Li, and N. El-Sheimy
Evaluation of two WiFi positioning systems based on autonomous crowdsourcing of handheld devices for indoor navigation
IEEE Trans. Mobile Comput., vol. 15, no. 8, pp. 1982–1995, Aug. 2016.

[28] Z. Kassas and T. Humphreys
Observability analysis of collaborative opportunistic navigation with pseudorange measurements
IEEE Trans. Intell. Transp. Syst., vol. 15, no. 1, pp. 260–273, Feb. 2014.

[29] J. Morales and Z. Kassas
Stochastic observability and uncertainty characterization in simultaneous receiver and transmitter localization
IEEE Trans. Aerosp. Electron. Syst., vol. 55, no. 2, pp. 1021–1031, Apr. 2019.

[30] Z. Kassas, A. Arapostathis, and T. Humphreys
Greedy motion planning for simultaneous signal landscape mapping and receiver localization
IEEE J. Sel. Topics Signal Process., vol. 9, no. 2, pp. 247–258, Mar. 2015.

[31] Z. Kassas and T. Humphreys
Receding horizon trajectory optimization in opportunistic navigation environments
IEEE Trans. Aerosp. Electron. Syst., vol. 51, no. 2, pp. 866–877, Apr. 2015.

[32] C. Yang and A. Soloviev
Positioning with mixed signals of opportunity subject to multipath and clock errors in urban mobile fading environments
In *Proc. ION GNSS Conf.*, 2018, pp. 223–243.

[33] C. Yang, T. Nguyen, E. Blasch, and D. Qiu
Assessing terrestrial wireless communications and broadcast signals as signals of opportunity for positioning and navigation
In *Proc. ION GNSS Conf.*, Sep. 2012, pp. 3814–3824.

[34] C. Yang, T. Nguyen, and E. Blasch
Mobile positioning via fusion of mixed signals of opportunity
IEEE Aerosp. Electron. Syst. Mag., vol. 29, no. 4, pp. 34–46, Apr. 2014.

[35] M. Driusso, C. Marshall, M. Sabathy, F. Knutti, H. Mathis, and F. Babich
Vehicular position tracking using LTE signals
IEEE Trans. Veh. Technol., vol. 66, no. 4, pp. 3376–3391, Apr. 2017.

[36] K. Shamaei, J. Khalife, and Z. Kassas
Exploiting LTE signals for navigation: Theory to implementation
IEEE Trans. Wireless Commun., vol. 17, no. 4, pp. 2173–2189, Apr. 2018.

[37] J. Khalife and Z. Kassas
Precise UAV navigation with cellular carrier phase measurements
In *Proc. IEEE/ION Position, Location, Navigation Symp.*, Apr. 2018, pp. 978–989.

[38] J. Khalife, K. Shamaei, S. Bhattacharya, and Z. Kassas
Centimeter-accurate UAV navigation with cellular signals
In *Proc. ION GNSS Conf.*, Sep. 2018, pp. 2321–2331.

[39] Z. Kassas, J. Morales, K. Shamaei, and J. Khalife
LTE steers UAV
GPS World Mag., vol. 28, no. 4, pp. 18–25, Apr. 2017.

[40] Z. Kassas, M. Maaref, J. Morales, J. Khalife, and K. Shamaei
Robust vehicular localization and map matching in urban environments through IMU, GNSS, and cellular signals
IEEE Intell. Transp. Syst. Mag., vol. 12, no. 3, pp. 36–52, Jun. 2020.

[41] H. Durrant-Whyte and T. Bailey
Simultaneous localization and mapping: Part I
IEEE Robot. Automat. Mag., vol. 13, no. 2, pp. 99–110, Jun. 2006.

[42] C. Yang and A. Soloviev
Simultaneous localization and mapping of emitting radio sources-SLAMERS
In *Proc. ION GNSS Conf.*, Sep. 2015, pp. 2343–2354.

[43] J. Morales, P. Roysdon, and Z. Kassas
Signals of opportunity aided inertial navigation
In *Proc. ION GNSS Conf.*, Sep. 2016, pp. 1492–1501.

[44] J. Morales and Z. Kassas
A low communication rate distributed inertial navigation architecture with cellular signal aiding
In *Proc. IEEE Veh. Technol. Conf.*, 2018, pp. 1–6.

[45] J. Morales, J. Khalife, and Z. Kassas
GNSS vertical dilution of precision reduction using terrestrial signals of opportunity
In *Proc. ION Int. Tech. Meeting Conf.*, Jan. 2016, pp. 664–669.

[46] J. Khalife and Z. Kassas
Opportunistic UAV navigation with carrier phase measurements from asynchronous cellular signals
IEEE Trans. Aerosp. Electron. Syst., vol. 56, no. 4, pp. 3285–3301, Aug. 2020.

[47] J. Farrell and M. Barth
Aided Navigation: GPS With High Rate Sensors
New York, NY, USA: McGraw-Hill, 2008.

[48] P. Groves
Principles of GNSS, *Inertial, and Multisensor Integrated Navigation Systems*
2nd ed. Norwood, MA, USA: Artech House, 2013.

[49] M. Braasch
Inertial Navigation Systems, in Aerospace Navigation Systems
Hoboken, NJ, USA: Wiley, 2016.

[50] D. Gebre-Egziabher
What is the difference Between 'loose, 'tight', 'ultra-tight' and 'deep' integration strategies for INS and GNSS"Inside GNSS, pp. 28–33, Jan. 2007.

[51] R. Brown and P. Hwang
Introduction to Random Signals and Applied Kalman Filtering 3 rd ed. Hoboken, NJ, USA: Wiley, 1996.

[52] A. Thompson, J. Moran, and G. Swenson
Interferometry and Synthesis in Radio Astronomy
2nd ed. Hoboken, NJ, USA: Wiley, 2001.

[53] R. Snay and M. Soler
Continuously operating reference station (CORS): History, applications, and future enhancements
J. Surveying Eng., vol. 134, no. 4, pp. 95–104, Nov. 2008.

[54] M. Braasch and A. van Dierendonck
GPS receiver architectures and measurements
Proc. IEEE Proc. IRE, vol. 87, no. 1, pp. 48–64, Jan. 1999.

[55] S. Tay and J. Marais
Weighting models for GPS pseudorange observations for land transportation in urban canyons
In *Proc. Eur. Workshop GNSS Signals Signal Process.*, Dec. 2013.

[56] J. Liberti and T. Rappaport
A geometrically based model for line-of-sight multipath radio channels
In *Proc. IEEE Veh. Technol. Conf.*, Apr. 1996, vol. 2, pp. 844–848.

[57] J. Khalife, K. Shamaei, and Z. Kassas
Navigation with cellular CDMA signals - Part I: Signal modeling and software-defined receiver design
IEEE Trans. Signal Process., vol. 66, no. 8, pp. 2191–2203, Apr. 2018.

[58] M. Maaref and Z. Kassas
Measurement characterization and autonomous outlier detection and exclusion for ground vehicle navigation with cellular signals
IEEE Trans. Intell. Veh., vol. 5, no. 4, pp. 670–683, Dec. 2020.

[59] J. Morales and Z. Kassas
Distributed signals of opportunity aided inertial navigation with intermittent communication
In *Proc. ION GNSS Conf.*, Sep. 2017, pp. 2519–2530.

[60] Autel Robotics, Bothell, WA , USA. [Online]. Available: https://auteldrones.com

[61] *Ettus Research Tri-Band Antenna*
Austin, TX, USA, 2020. [Online]. Available: www.ettus.com/all-products/vert400

[62] *GPS Active Antenna*
QGP Supply, Kansas City, MO, USA, 2020.

[63] Universal Software Radio peripheral-2954R
National Instruments, Austin, TX, USA.

[64] J. Morales and Z. Kassas
Optimal collaborative mapping of terrestrial transmitters: Receiver placement and performance characterization
IEEE Trans. Aerosp. Electron. Syst., vol. 54, no. 2, pp. 992–1007, Apr. 2018.

[65] Y. Bar-Shalom, X. Li, and T. Kirubarajan
Estimation With Applications to Tracking and Navigation
New York, NY, USA: Wiley, 2002.

[66] K. Pesyna, Z. Kassas, J. Bhatti, and T. Humphreys
Tightly-coupled opportunistic navigation for deep urban and indoor positioning
In *Proc. ION GNSS Conf.*, Sep. 2011, pp. 3605–3617.

[67] Z. Kassas, V. Ghadiok, and T. Humphreys
Adaptive estimation of signals of opportunity
In *Proc. ION GNSS Conf.*, Sep. 2014, pp. 1679–1689.

[68] J. Farrell and M. Barth
Global Positioning System and Inertial Navigation
New York, NY, USA: McGraw-Hill, 1998.

Joshua J. Morales (Member, IEEE) received the B.S. in electrical engineering (Hon.) from the University of California, Riverside, CA, USA, and the Ph.D. in electrical engineering and computer science from University of California, Irvine (UCI), CA, USA.

He is a Principal with StarNav LLC. Previously he was a member of the Autonomous Systems Perception, Intelligence, and Navigation (ASPIN) Laboratory with the University of California, Irvine. His interests include estimation theory, navigation systems, autonomous vehicles, and cyber-physical systems.

In 2016, he was the recipient of the Honorable Mention from the National Science Foundation (NSF), and the National Center for Sustainable Transportation (NCST) Outstanding Graduate Student of the Year award, in 2018.

Zaher (Zak) M. Kassas (Senior Member, IEEE) received the B.E. degree in electrical engineering from the Lebanese American University, the M.S. degree in electrical and computer engineering from The Ohio State University, Columbus, OH, USA, and the M.S.E. degree in aerospace engineering and the Ph.D. degree in electrical and computer engineering from the University of Texas at Austin, TX, USA.

He is an Associate Professor with the University of California, Irvine, CA, USA, and Director of the Autonomous Systems Perception, Intelligence, and Navigation (ASPIN) Laboratory. He is also the Director of the U.S. Department of Transportation Center: CARMEN (Center for Automated Vehicle Research with Multimodal AssurEd Navigation), focusing on navigation resiliency and security of highly automated transportation systems. His research interests include cyber-physical systems, estimation theory, navigation systems, autonomous vehicles, and intelligent transportation systems.

He was the recipient of the 2018 National Science Foundation (NSF) Faculty Early Career Development Program (CAREER) award, and 2019 Office of Naval Research (ONR) Young Investigator Program (YIP) award. He was also a recipient of the 2018 IEEE Walter Fried Award, 2018 Institute of Navigation (ION) Samuel Burka Award, and 2019 the Institute of Navigation (ION) Col. Thomas Thurlow Award. He is an Associate Editor for the IEEE TRANSACTIONS ON AEROSPACE AND ELECTRONIC SYSTEMS and IEEE TRANSACTIONS ON INTELLIGENT TRANSPORTATION SYSTEMS.